EPITAXIAL GROWTH OF Bi-Sr-Ca-Cu-O SUPERCONDUCTING FILM ON MgO BY THE THE COMBINED METHOD OF POWDER DEPOSITION AND LIQUID PHASE SINTERING AND ANNEALING TECHNIQUE

ADREL VOLTAIRE ARCEO CUETO

NATIONAL INSTITUTE OF PHYSICS
College of Science
University of the Philippines
Diliman, Quezon City

SEPTEMBER 2003

Epitaxial Growth of Bi-Sr-Ca-Cu-O Superconducting Film on MgO by the Combined Method of Powder Deposition and Liquid Phase Sintering and Annealing Technique

Adrel Voltaire Arceo Cueto

An Undergraduate Thesis Submitted to the
National Institute of Physics
College of Science
University of the Philippines
Diliman, Quezon City

As Partial Fulfillment of the Requirements
For the Degree of
BACHELOR OF SCIENCE IN APPLIED PHYSICS

24 SEPTEMBER 2003

NATIONAL INSTITUTE OF PHYSICS
COLLEGE OF SCIENCE
UNIVERSITY OF THE PHILIPPINES
DILIMAN, QUEZON CITY 1101
PHILIPPINES
TEL. NOS. 9205301 TO 99 Loc. 6431/6846/6312
FAX NO. 920-5474

ANNOUNCEMENT OF THE UNDERGRADUATE THESIS SEMINAR

of

ADREL VOLTAIRE ARCEO CUETO

on

"EPITAXIAL GROWTH OF Bi-Sr-Ca-Cu-O SUPERCONDUCTING FILM ON MgO BY THE COMBINED METHOD OF POWDER DEPOSITION AND LIQUID PHASE SINTERING AND ANNEALING TECHNIQUE"

in partial fulfillment of the requirements for the degree of
BACHELOR OF SCIENCE IN APPLIED PHYSICS
on Wednesday, 24 September 2003, NIP Audio-Visual Room at 3:00pm

THESIS ADVISER

ROLAND V. SARMAGO, Ph.D.
Professor of Physics
National Institute of Physics
College of Science, U.P. Diliman

THESIS EXAMINER

ARNEL A. SALVADOR, Ph.D.
Professor of Physics
National Institute of Physics
College of Science, U.P. Diliman, Q.C.

THESIS EXAMINER

HENRY J. RAMOS, Ph.D.
Professor of Physics
National Institute of Physics
College of Science, U.P. Diliman, Q.C.

ENDORSED BY:

RONALD S. BANZON, Ph.D.
Deputy Director for Academic Affairs
National Institute of Physics
College of Science, U.P. Diliman, Q.C.

AUTHORIZED BY:

CAESAR A. SALOMA, Ph.D.
Director of Institute
National Institute of Physics
College of Science, U.P. Diliman, Q.C.

NATIONAL INSTITUTE OF PHYSICS
COLLEGE OF SCIENCE
UNIVERSITY OF THE PHILIPPINES
DILIMAN, QUEZON CITY 1101
PHILIPPINES

TEL. NOS. 9205301 to 99 Loc. 6431/6846/6312
FAX NO. 920-5474

September 24, 2003

Dr. Caesar A. Saloma
Director of Institute
National Institute of Physics
C.S., U.P. Diliman, Quezon City

Dear Dr. Saloma:

Below is the official action of the panel members in the undergraduate thesis defense of Mr. Adrel Voltaire A. Cueto. The defense of thesis entitled "**Epitaxial Growth of BSCCO Superconducting Film on MgO by the Combined Method of Powder Deposition and Liquid Phase Sintering and Annealing Technique**", was held at PH 3213, Wednesday, 24 September 2003, 3:00 P.M.

Panel Members	Rating PASSED	 FAILED
Dr. Arnel A. Salvador Professor of Physics National Institute of Physics C.S., U.P. Diliman, Quezon City		
Dr. Henry J. Ramos Professor of Physics National Institute of Physics C.S., U.P. Diliman, Quezon City		
Dr. Roland V. Sarmago (Adviser) Professor of Physics National Institute of Physics C.S., U.P. Diliman, Quezon City		

The rating is therefore passed.

Sincerely yours,

RONALD S. BANZON, Ph.D.
Deputy Director for Academic Affairs

This is to certify that this undergraduate thesis, entitled "**Epitaxial Growth of Bi-Sr-Ca-Cu-O Superconducting Film on MgO by the Combined Method of Powder Deposition and Liquid Phase Sintering and Annealing Technique**" and submitted by **Adrel Voltaire Arceo Cueto** to fulfill part of the requirements for the degree of *Bachelor of Science in Applied Physics*, was successfully defended and approved on 24 September 2003.

ROLAND V. SARMAGO, Ph.D.
Thesis Adviser
Professor of Physics
National Institute of Physics
College of Science, U.P. Diliman
Quezon City

Arnel Salvador

ARNEL A. SALVADOR, Ph.D.
Panel Member
Professor of Physics
National Institute of Physics
College of Science, U.P. Diliman
Quezon City

HENRY J. RAMOS, Ph.D.
Panel Member
Professor of Physics
National Institute of Physics
College of Science, U.P. Diliman
Quezon City

The National Institute of Physics endorses acceptance of this undergraduate thesis as partial fulfillment of the requirements for the degree of Bachelor of Science in Applied Physics.

CAESAR A. SALOMA, Ph.D.
Director
National Institute of Physics
College of Science, U.P. Diliman
Quezon City

The undergraduate thesis is hereby officially accepted as partial fulfillment of the requirements for the degree of Bachelor of Science in Applied Physics.

RHODORA AZANZA, Ph.D.
Dean
College of Science, U.P. Diliman
Quezon City

AKNOWLEDGEMENTS

I would like to acknowledge the following people for their brilliant ideas, excellent works, and great companionship that in one way or another have inspired and contributed to the perfection of this work. I am deeply indebted... ☺

- **My thesis adviser**
  - Dr. Roland Sarmago
- **My thesis examiners**
  - Dr. Arnel Salvador
  - Dr. Henry Ramos
- **My thesis and seminar reviewers**
  - Bautista, Angel Kristine
  - Casco, Frantessa
  - Cruz, Minerva
  - Cureg, Rommel
  - De la Cruz, Clarina
  - Dela Cruz, Aaron Paul
  - Guerra, Leandro Jose
  - Hinojales, Ervinjon
  - Herrera, Marvin
  - Manuel, Ayn Hazel
  - Podpod, Arnita
- **My SEM images**
  - Baustista, Angel Kristine
  - Manuel, Ayn Hazel
  - Pascua, Gwendolyn
  - Rillera, Hannah
  - La Salle SEM facility
- **My XRD scans**
  - Bautista, Angel Kristine
  - Guiao, Luisito
  - Manuel, Ayn Hazel
  - Podpod, Arnita
- **My Resistivity Measurements**
  - Dela Cruz, Aaron Paul
  - Dumlao, Geraldine
  - Hinojales, Ervinjon
  - Ronulo, Jonathan
- **My seminar audience**
  - CMPL kidz
  - Class of Dr. Saloma
  - NIP community
- **My Labmates**
  - Afalla, Jesica
  - Ambanta, Ivan-Ronald
  - Bernaldez, Loraine
  - Blanca , Gaiza
  - Bugante, Jan
  - Dazo, Lorelai
  - Dela Cruz, Aaron Paul
  - Dumlao, Geraldine
  - Espina, Dianne
  - Herrera, Marvin
  - Hinojales, Ervinjon
  - Manahan, Ruby
  - Mendoza, Portia
  - Olbinado, Margie
  - Pascua, Gwendolyn
  - Pigarowa, Stephanie
  - Ramos, Dominador
  - Rillera, Hannah
  - Ronulo, Jonathan
  - Sarmiento, Raniel
  - Sibayan-Torralba, Veronica
  - Singidas, Bess
  - Sioson, Remylou
  - Uy, Mylein
  - Yanson, Ivan
  - and the Semicon People
- **My Apprentices**
  - Manahan, Ruby
  - Sarmiento, Raniel
- **My batchmates**
  - Ambanta, Ivan-Ronald
  - Bernaldez, Loraine
  - Dela Cruz, Aaron Paul
  - Hinojales, Ervinjon
- **My Support Group**
  - Baustista, Angel
  - Dela Cruz, Aaron Paul
  - Hinojales, Ervinjon
  - Llena, Mark
  - Manuel, Ayn
  - Podpod, Arnita
  - Rillera, Hannah
  - Sarmiento, Raniel
- **My Bio Lab Classmates and Teacher**

To my Mom and Dad...

My most sincere thanks to you all! ☺

Table of Contents

Chapter 1: Significance of the Study 1

Reference 4

Chapter 2: Material Science of BSCCO Superconductors 5

2.1 BSCCO Superconductors 5

2.2 BSCCO Film Fabrication Processes 10

2.2.1 Liquid Phase Epitaxial Method 11

2.2.2 Magnetron Sputtering and Molecular Beam Epitaxy 12

2.2.3 Laser Ablation and Pulsed Laser Deposition 14

2.2.4 Ion Beam Sputtering and Thermal Coevaporation 15

2.2.5 Chemical Non-vacuum techniques 15

2.3 Present Fabrication Process 16

Reference 18

Chapter 3: Powder Characteristics and Liquid Phase Sintering and Annealing Processes 20

3.1 Powder Characteristics 20

3.2 Liquid Phase Annealing 21

3.2.1 Heating and Melting Stage 22

3.2.2 Solution-Reprecipitation Stage 22

3.2.3 Microstructural Coarsening 23

Reference 24

Chapter 4: Experimental Procedures 25

4.1 Film Production 25

4.1.1 Preparation of Bi2201, Bi-2212, and Bi-2223 Powder Precursors 25

4.1.2 Film Deposition 26

4.1.3 Film Heat Processing and Annealing 28

4.2 Film Characterization 29

4.2.1 X-Ray Diffraction 29

4.2.2 Scanning Electron Microscopy 31

4.2.3 Resistivity Measurements: The Four-Probe Technique 32

Reference 33

Chapter 5: Results and Discussions 34

5.1 Scanning Electron Microscopy Analysis 34

5.1.1 Initial Deposited Powder Characteristics 34

5.1.2 The Films After Liquid Phase Sintering and Annealing Process 35

5.2 X-Ray Diffraction Analysis 38

5.2.1 Film Orientation and *c*-Lattice Parameter Determination 38

5.2.1.1 XRD analysis of the $Bi_2Sr_2CuO_{6+\delta}$ (Bi-2201) film 38

5.2.1.2 XRD analysis of the $Bi_2Sr_2CaCu_2O_{8+\delta}$ (Bi-2212) film 41

5.2.1.3 Multi-phase $Bi_2Sr_2CaCu_2O_{8+\delta}$ (Bi-2212) and $Bi_2Sr_2Ca_2Cu_3O_{10+\delta}$ (Bi-2223) film 43

5.2.2 Extraneous X-Ray Peaks 45

5.2.3 BSCCO Relative Phases Determination 49

5.3 Superconducting Characteristics 51

5.4 Mechanism of Film Growth and Alignment 54

Reference 56

Chapter 6: Conclusions and Recommendations 57

Appendix A: XRD simulations 59

Appendix B: Bi-2212 optimal growth 72

Appendix C: Preliminary result of *c*-axis oriented YBCO film 75

Abstract

Highly *c*-axis oriented BSCCO films were successfully grown on MgO (0 0 1) single crystal substrate by the combined method of powder deposition technique and heat treatment via liquid phase sintering process. Relatively single-phased $Bi_2Sr_2CuO_{6+\delta}$ (Bi-2201) and $Bi_2Sr_2CaCu_2O_{8+\delta}$ (Bi-2212) were obtained by this simple film fabrication method. Multi-phase film, composed of Bi-2212 and $Bi_2Sr_2Ca_2Cu_3O_{10+\delta}$ (Bi-2223), was also obtained in an attempt to produce single phased Pb-free Bi-2223 superconducting film. Surface morphology and the crystal structure were analyzed with scanning electron microscopy and x-ray diffraction method. The thickness of the films was measured to be 13 microns. Superconductivity of the films was confirmed using standard four-probe resistivity measurement. Critical temperatures of 17 K, 90 K and 108 K, were determined for the Bi-2201, Bi-2212 and Bi-2223 respectively. Mechanism of the film growth was also discussed based on the x-ray diffraction analysis and scanning electron microscopy images of the film samples.

Chapter 1

Significance of the Study

Developments in the field of superconductivity are intimately related to the progress in materials research, particularly for High Temperature Superconductors (HTSC). In the attempt to utilize the science and technology of these superconducting materials, a lot of works have been put into the processing and optimization of superconducting properties for future applications. Possible use of HTSC materials can be subdivided into two main areas; first are the large scale energy-related applications such as in generation, transport, transformation and storage of electrical power and second are small-scale electronics-related applications such as passive and active signal processing [1]. Future superconductor applications will require advanced preparation and characterization technologies, down to the nanometer scale. It is therefore substantial to put strong efforts in materials research both at the laboratory and industrial scale.

Among the high-Tc superconducting materials that have been of interest since its discovery is the Bi-Sr-Ca-Cu-O (BSCCO) system. The BSCCO system was first discovered by Maeda *et al.* [2] and is known to have three superconducting phases: the $Bi_2Sr_2CuO_{6+\delta}$ (Bi-2201) with Tc~20 K, $Bi_2Sr_2CaCu_2O_{8+\delta}$ (Bi-2212) with Tc~80 K and $Bi_2Sr_2Ca_2Cu_3O_{10+\delta}$ (Bi-2223) with Tc~110 K. Great efforts have been put into the processing and study of these challenging compounds, with emphasis on the fabrication of single phased samples. While single phased Bi-2201 and Bi-2212 can be easily obtained, single phased Bi-2223, has been proven to be very difficult to produce. The difficulty lies in and is evidenced by the complexities of the phase diagrams of the high-temperature superconducting phases of the BSCCO system [3].

For almost 15 years, the Bi-2223 phase has been proven to be difficult to obtain in a single phased form. Almost every published paper focused on optimizing the amount of Bi-2223 superconducting phase in the multiphase samples. Others do research on electronic characteristics, microstructure, texture, and impurity phases. Despite these complexities, however, the BSCCO system still has stimulated worldwide research activities up to now. Much focus is on the 2223 phase, which has the highest critical temperature of 110K among the BSCCO phases. One characteristic of 2223 phase is its far better superconducting capability due to its higher critical temperature compared to its counterpart superconducting material YBCO, T_c~95K. Also, BSCCO materials are non-toxic in contrast to the higher T_c materials presently known, e.g. Hg and Tl-based superconducting materials. However, the problem of obtaining high quality Bi2223 superconductors is substantial and still far from being solved.

In terms of superconducting film production, various techniques such as Liquid Phase Epitaxy, RF-Magnetron Sputtering, Pulsed Laser Deposition, are among the well-known method used. Initial attempts in the fabrication of BSCCO films in the Condensed Matter Physics Laboratory involved the use of LPE furnace. In this method, a mixture of BSCCO and KCl flux is placed in a furnace resulting to a melt solution. It is then followed by MgO dipping unto the melt to facilitate formation of the film. The method, however, does not yield a reproducible and good quality BSCCO film, particularly the Bi-2223 phase due to its narrow stability temperature range. Bi-2223 is also known to decompose at melting temperature thus resulting to a lower success rate in solution growth of Bi2223. Furthermore, in solution growth, the bulk of the material (melt residue) usually goes to waste.

The purpose of this work is to propose a relatively simple technique of epitaxial film production using the combined processes of liquid-assisted powder deposition and liquid phase sintering and annealing method. The powder deposition process is simple in a sense that no complicated equipment is used. It utilizes the effect of dispersant liquid to evenly distribute the powder on the surface of MgO substrate as the liquid evaporates. This evaporation of the liquid will result to a film of deposited powder on MgO substrate. BSCCO powder is used for this purpose in film fabrication.

Film alignment is a major goal in processing high- T_c material for applications requiring high currents. To achieve a good epitaxial BSCCO film, liquid phase sintering and annealing technique is employed. Compared to LPE furnace previously used in the laboratory, preliminary result suggests good quality epitaxial films and almost perfectly reproducible samples. Also, quantifying the amount of powder to be deposited may control the desired thickness of the film sample in this present technique. However, the thickness relation with the amount of deposited powder is beyond the scope of this work. A possible mechanism of growth is also discussed based on the X Ray diffraction pattern and scanning electron microscope image of the film.

Reference:

[1] M. Marezio. "Superconducting Materials" Material Science and Application

[2] H. Maeda. Y. Tanaka, M. Fukutomi and T. Asano: Jpn. J. Appl. Phys. 27 (1988) L209

[3] Majewski P. "Materials aspects of the high-temperature superconductors in the system Bi_2O_3-SrO-CaO-CuO", J. Mater. Res., Vol. 15, No. 4, Apr. 2000

Chapter 2
Materials Science of BSCCO Superconductors

2.1 Bi-Sr-Ca-Cu-O Superconductors

The Bi-Sr-Ca-Cu-O (BSCCO) system consists of three different superconducting phases: $Bi_2Sr_2CuO_{6+\delta}$ (Bi-2201), $Bi_2Sr_2CaCu_2O_{8+\delta}$ (Bi-2212) and $Bi_2Sr_2Ca_2Cu_3O_{10+\delta}$ (Bi-2223), with critical temperatures of about 20, 80 and 110 K, respectively. The delta (δ) signifies that the oxygen content varies depending on the oxygen doping level imposed on the sample. The general chemical formula for the homologous series of these bismuth compounds is $Bi_2Sr_2Ca_{n-1}Cu_nO_{2n+4}$, where n (n=1,2,3), that denotes the number of CuO_2 planes. With five elements involved, the Bi-Sr-Ca-Cu-O system is complex, and its phase diagram is not well understood. Since its discovery in 1988 by Maeda *et al.* [1], interests worldwide focused on the processing and optimization particularly in formation between 2212 and 2223 phases. The Bi2212 phase can be easily prepared in almost pure phase since it is thermodynamically stable in a wide range of temperature. The synthesis of Bi-2223 phase however has been proven to be difficult and usually does not allow one to obtain a pure phase. It was found that addition of small amount of Pb promotes and stabilizes the Bi-2223 phase [2]. Excessive Pb however favors the appearance of the Ca_2PbO_4 phase that assists the formation of Bi-2212 [3]. Any mechanism proposed for the transformation of Bi-2212 to Bi-2223 is accepted unanimously as summarized by V. Garnier [4];

- A disproportionation reaction of the Bi(Pb)-2212 phase to form the Bi-2223 and Bi-2201 phases

- An intercalation process in which the pre-existing Bi(Pb)-2223 crystals transform directly in Bi(Pb)-2223 platelets via the insertion of the CuO_2/Ca bilayers into the CuO_2/Ca/CuO_2 blocks of Bi-2212
- Formation of Bi/Pb rich mobile liquid droplets which migrate over growing platelets
- A dissolution precipitation process where the Bi-2223 phase is formed from both the Bi-2212 phase, CaO, and a liquid, the last two components arising from the decomposition of Ca_2PbO_4
- A two-dimensional growth with decreasing nucleation rates. A liquid phase generated in the powder reacts with the Bi-2212 matrix via the diffusion of Ca, Cu and Pb ions, resulting in the nucleation of the Bi-2223, which diffuses into the Bi-2212 matrix, maintaining the outline of the original crystal shape

The BSCCO compounds have complex layered structures parallel to the crystallographic a,b plane, as illustrated in Figure 2.1, consisting of rocksalt-like BiO bilayers that alternate in *c* direction with perovskite-like $Sr_2Ca_{n-1}Cu_nO_{1+2n}$ units [5]. This perovskite-like structure with the CuO planes can be found in almost every high T_c materials, with few exceptions, and believed to be the conduction planes for the superconducting current. The other layer, BiO bi-layers, is believed to act as a charge reservoir, donating holes to the superconducting copper oxide planes. BSCCO unit cells are nearly tetragonal, with significant difference on the length of the *c*-axis. In Bi-2201, the lowest temperature phase, has no calcium layer in between the perovskite structure and with c=24.4 Å. Additional layer of CaO in the CuO plane of Bi-2212 have contributed to the increase in the *c*-lattice to 30.7 Å. The longest *c*-lattice is the Bi-2223 with 36.7 Å due to the layer CaO-CuO-CaO sandwiched in between the CuO_2 octahedral layer. Listed in Table 2.1 are the crystal lattice parameters of the BSCCO phases. Notice also that the transition temperature rises with increasing number of CuO_2 planes from n=1 to n=3.

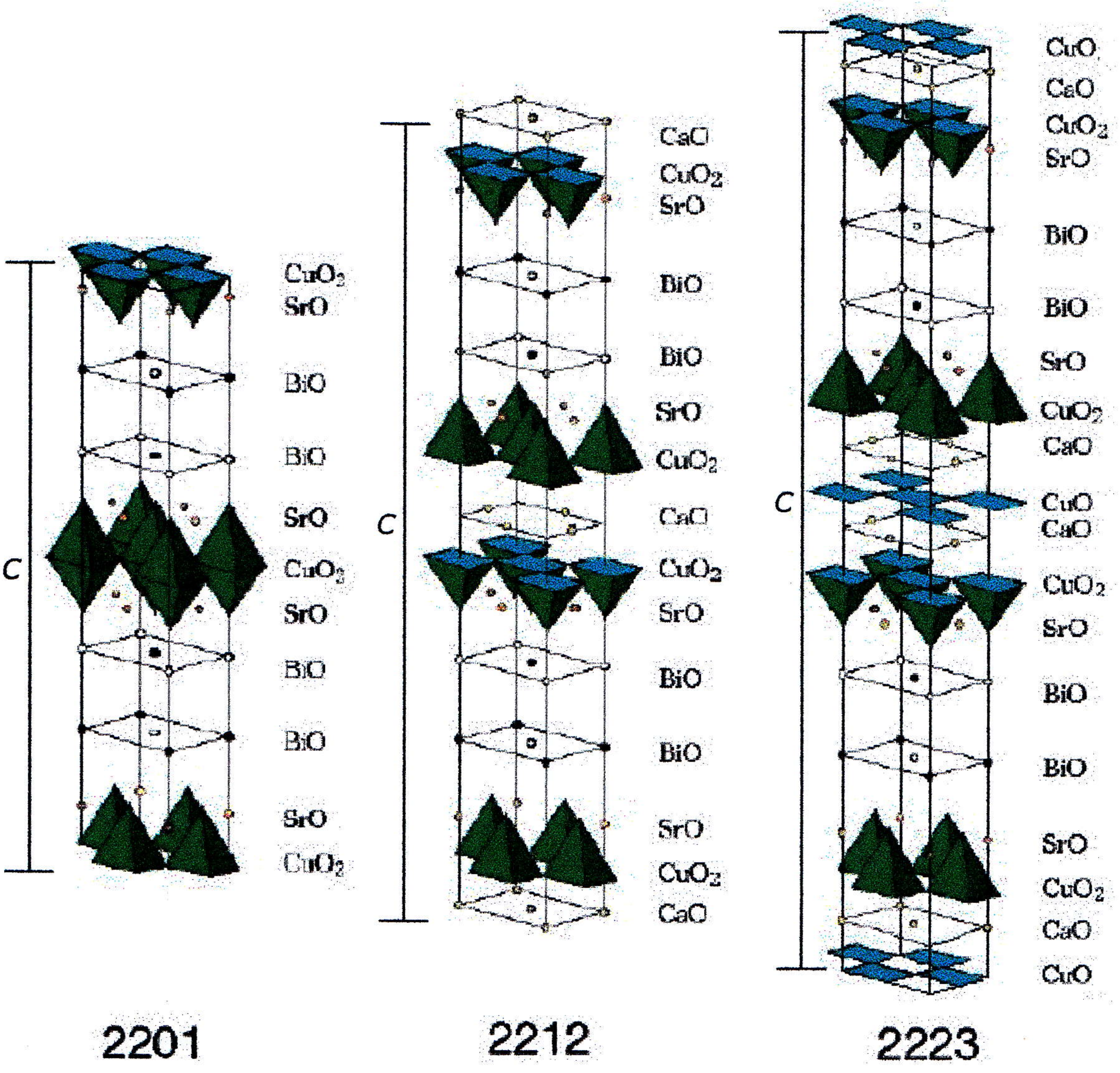
CuO2
SrO
BiO
BiO
SrO
CuO2
SrO
BiO
BiO
SrO
CuO2
C
2201
CaO
CuO2
SrO
BiO
BiO
SrO
CuO2
CaO
CuO2
SrO
BiO
BiO
SrO
CuO2
CaO
C
2212
CuO
CaO
CuO2
SrO
BiO
BiO
SrO
CuO2
CaO
CuO
CaO
CuO2
SrO
BiO
BiO
SrO
CuO2
CaO
CuO
C
2223

Figure 2.1 *Crystal Structures of BSCCO Phases.*

Table 2.1. *Lattice constants and transition temperatures of BSCCO phases.*

BSCCO phases	***a*** (Å)	***b*** (Å)	***c*** (Å)	***T$_c$*** (K)
Bi-2201	~5.4	~5.4	~24.4	~20
Bi-2212	~5.4	~5.4	~30.7	~80
Bi-2223	~5.4	~5.4	~36.7	~110

BSCCO structures also exhibit an incommensurate modulation in the direction of the crystallographic *b* axis. The modulated structures are difficult to study by conventional X-ray and neutron diffraction techniques, so most of the information was obtained by electron microscopic methods [8,9]. Majewski reported this superstructure as revealed by TEM image with spacing of about 4.47 times that of the *b*-axis parameter with the space group *Pcnn* or *Pmnn* [7]. This superstructure is formed by a modulation of the BiO bilayers, which results in a regular alternation of the structure of the BiO bilayers. Although it is not yet clarified, the modulation of the BiO bilayers may be due to either excess oxygen in the BiO layers causing Bi^{5+} or to a poor match between the BiO bilayers with a Bi-O bond length of 0.212-0.215 nm and the perovskite-like $Sr_2Ca_{n-1}Cu_nO_{1+2n}$ units with a CuO bond length of 0.1914 nm.

This structure also implies a pronounced anisotropy of the properties, causing the so-called "two dimensional superconductivity" parallel to the *a,b* plane. Due to the anisotropic crystal structure of BSCCO materials, its effect on the crystal growth is a much higher growth velocity along the *a,b* plane than in the *c* direction. This explains why the BSCCO microcrystals grow as thin platelets several hundred microns in size along the *ab* plane and less than ten microns in size in the *c* direction. Also, as a consequence of this anisotropy, the electrical conductivity along the *ab* plane is higher than along the *c* axis [6].

Considerable effort has been done to be able to produce pure single phase BSCCO material. In order to do this, one has to understand the fundamental knowledge of materials regarding the processing and reactions. This can be worked out by studying the phase equilibria diagrams, which should basically provide a theoretical understanding about the phase relations and processing. However, phase diagrams for the BSCCO system have been a major problem due to its complexity. As the number of components in a system increases, the complexity involved in visualizing the phase diagrams becomes less manageable. A simple temperature vs. concentration phase diagram done by P. Majewski is shown in Figure 2.2 [7]. It shows the stability ranges of the superconducting phases and the relations with the superconducting phases of the BSCCO system. The Bi-2212 phase is stable up to 895°C and melts incongruently,

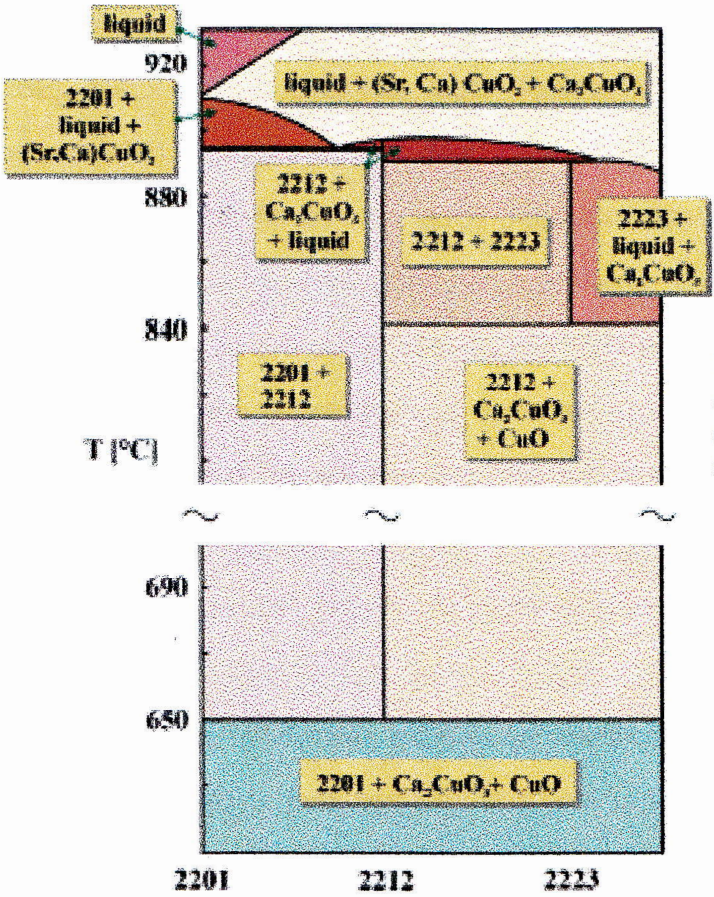

Figure 2.2. *Phase relation diagram of temperature vs. concentration between the range from Bi-2201 to Bi-2223 [7].*

meaning that the composition of the melt differs from that of the solid Bi-2212. The Bi-2223 phase is stable only within a narrow range of temperature of about 50°C. The Bi-2201 melting point was determined to be 910°C [7].

2.2 BSCCO Film Fabrication Processes

High T_c thin film fabrication is geared towards electronic device components, including sensors and microwave applications. Various preparation methods of BSCCO films have been published from the time of its discovery. The manufacturing techniques that are established in semiconductor device technology have been adapted to produce high T_c films. Some of these manufacturing techniques are molecular beam epitaxy (MBE), metal-organic chemical vapor deposition (MOCVD), RF sputtering, liquid phase epitaxy (LPE) and pulsed-laser deposition (PLD), all of which have been developed for fabricating BSCCO films. For each deposition method, routes for optimization have always been the prerequisites for satisfying the commercial use of film-based applications. Basic principles of superconducting thin film fabrication are common both to those governing polycrystalline materials processing and to those governing single crystal growth, but some important features have been carefully examined in thin film processing. It is generally assumed that high T_c thin films should, if properly prepared, have properties approaching those measured in single crystals [10].

Thin films for devices have to be reproducible, with transition temperature close to those observed in bulk material and with comparable transition widths. Success in these goals depends on the selection of compatible substrates [10]. In the choice of substrate material, the best substrates are that of perovskite-like structure such as $NdGaO_3$, $LaAlO_3$, and SrTiO3 where lattice mismatch with the BSCCO material is only about 1.20%, -0.72% and 2.3% respectively [12]. While these materials have perfectly matched BSCCO lattice for epitaxial growth, some materials show ferroelectric transitions that make them unusable in microwave applications. Surprisingly, MgO is a good substrate material, however it has a bad mismatch of 9.86% [12]. Although it has a bad lattice matching, BSCCO material is known to grow perfectly on MgO with c-axis orientation. Also, employing the heat treatment process on powder deposited sample is observed to make a good wetting between BSCCO and MgO material, which aids in the formation of epitaxially grown films.

In the succeeding paragraphs, several deposition techniques will be discussed in fabrication of high T_c superconductor thin films.

2.2.1 Liquid Phase Epitaxial Method

Liquid phase epitaxy (LPE) has become an important method of film growth, primarily because of its importance to the electronics industry. A wide variety of techniques have been devised to implement the LPE process, including variations in both the process method and equipment design. Whichever is the case, the objective is to transport the melt solution made to contact with the substrate material. In production of BSCCO film using the LPE method, starting materials are usually powders of Bi_2O_3, $SrCO_3$, $CaCO_3$, and CuO. KCl flux is usually used to reduce melting temperature of the mixture. It is then followed by MgO dipping unto the melt to facilitate formation of the film. A typical LPE furnace is illustrated in figure 2.3.

Figure 2.3. *Illustration of typical LPE furnace where BSCCO film is grown by dipping the single crystal MgO substrate into the solution.*

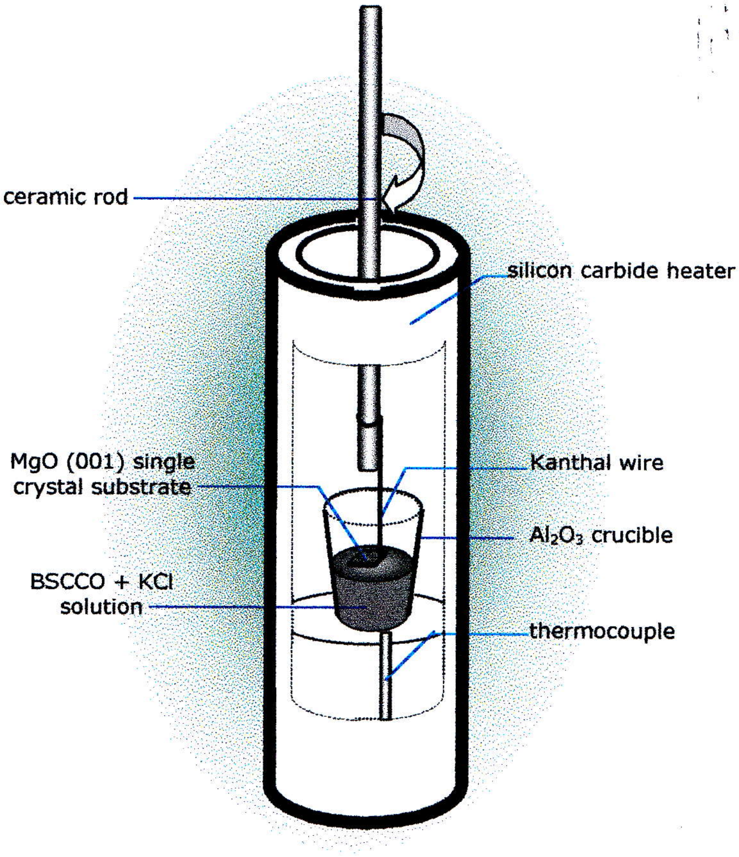
ceramic rod
silicon carbide heater
MgO (001) single crystal substrate
Kanthal wire
Al_2O_3 crucible
BSCCO + KCl solution
thermocouple

2.2.2 Magnetron Sputtering and Molecular Beam Epitaxy

Magnetron sputtering and Molecular Beam Epitaxy (MBE) have been shown to produce high quality films: these techniques appear to be suited mainly for thin films and/ or investigation of new hybrid structures, multilayers and devices. The thickness of grown thin films with these techniques usually ranges from 0.1-100 μm.

Sputter deposition of thin films is carried out at pressures, from 1 to 100 Pa with working inert gas, usually argon, introduced in the sputtering chamber. It is usually performed either with a single target or with multiple targets. The required small targets can be prepared by sintered mixtures of fine powders of Bi, Sr, Ca, Cu oxides and carbonates in appropriate composition ratio, and stoichiometry is retained from the target to the film. The deposition is usually followed by post annealing of the films to various temperature for optimum superconductivity characteristics. Multiple targets are utilized to precisely control the deposition composition since the phases of as-grown films changes with deposition conditions such as film composition and growth temperature [11].

The MBE occurs layer by layer, controlled by shutters as shown in Figure 2.4. Artificial compounds, not realized in bulk form, can be fabricated. For epitaxial growth, the specimen substrate is mounted to a heated holder and is tilted toward each furnace in turn during evaporation. Deposition rates are monitored by a flux gauge mounted behind the specimen. To grow films in situ, oxygen is bled into the chamber and a

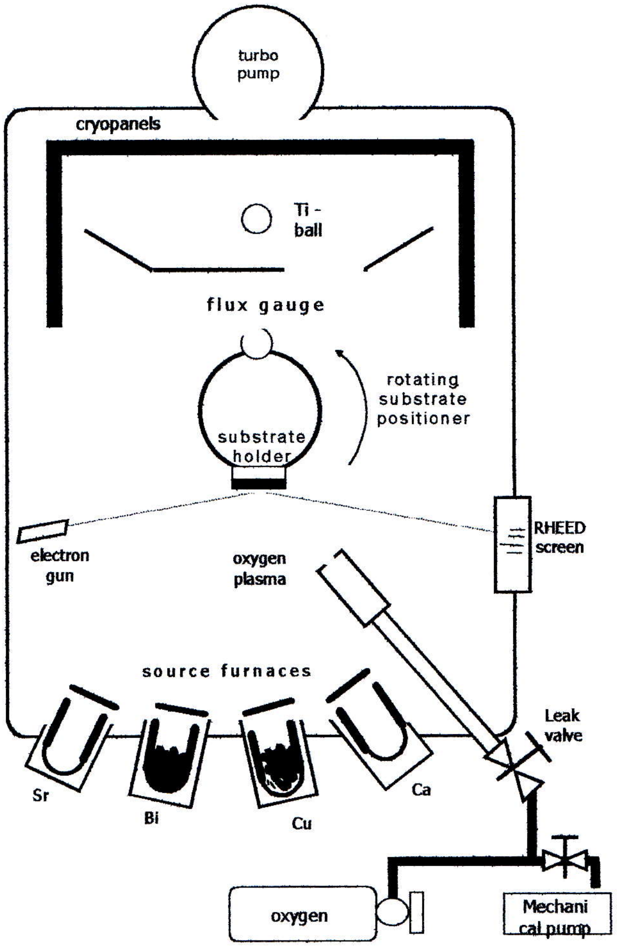
turbo pump
cryopanels
Ti - ball
flux gauge
rotating substrate positioner
substrate holder
electron gun
oxygen plasma
RHEED screen
source furnaces
Leak valve
Sr
Bi
Cu
Ca
oxygen
Mechani cal pump

Figure 2.4. *Illustration of typical molecular beam epitaxy deposition system of Bi-Sr-Ca-Cu-O.*

plasma formed by high tension discharge close to the specimen and substrate. The atomic structure of the film is monitored by reflection high energy electron diffraction (RHEED) of electrons directed towards the specimen at a glancing angle from an electron gun [10].

2.2.3 Laser Ablation and Pulsed Laser Deposition

Laser ablation and pulsed laser deposition, which are widely used in research laboratories, are powerful tools for synthesis and preliminary investigations of new phases. This method can also be applied for the fabrication of long tapes [13]. Thickness of the film usually ranges from 10-300 nm [14].

Figure 2.5 illustrates a typical experimental arrangement of laser ablation thin film deposition system. When a pulsed excimer laser, with an energy fluence about

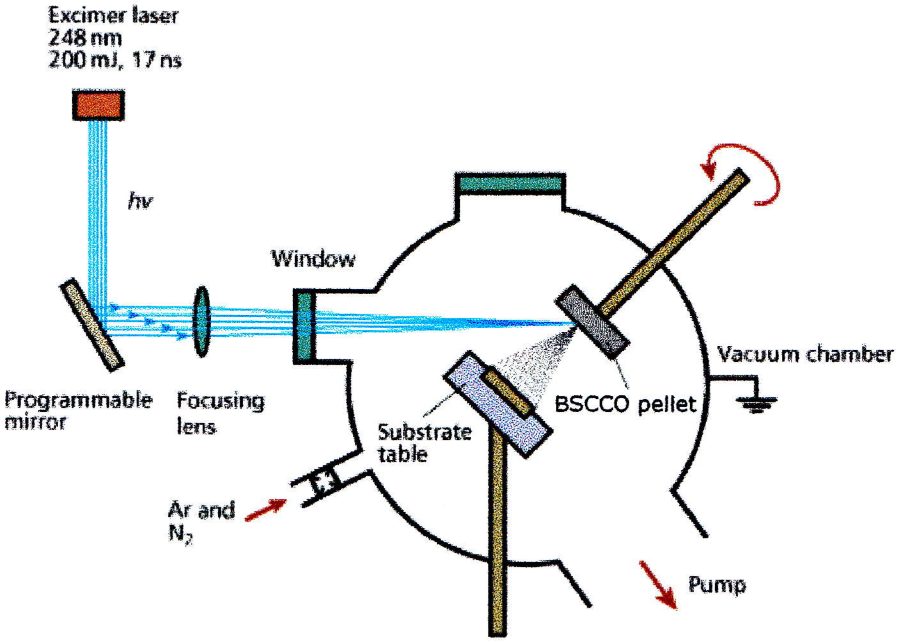
Excimer laser
248 nm
200 mJ, 17 ns
hv
Window
Programmable mirror
Focusing lens
Substrate table
BSCCO pellet
Vacuum chamber
Ar and N_2
Pump

Figure 2.5. *Experimental setup of typical laser ablation thin film deposition system.*

3J/cm^2 is focused onto target material, ablated species including atoms, molecules and radicals are transferred to the nearby substrate. The laser is contained outside the chamber with the entry window for laser beam often shielded from ejected material. The pressures of reactive gases, such as O_2 or N_2O, are adjustable and may be as high as 0.5 atm. The substrate is normally heated to enable epitaxial film growth. Deposition rates up to 10 nm/s are obtainable in high quality films. The deposition rate depends on the pulse repetition rate, which simply depends on what is commercially available. Each pulse of laser energy causes localized melting and evaporation, and leaves a crater in the target. The crater contains resolidified melt with various phases, so the target is moved between pulses to preserve stoichiometry in the deposited film. If the target is made of porous material, particulates are ablated and deposited on the substrate along with atoms, molecules and radicals. The deposition of particulates is alleviated by the use of dense targets [10].

2.2.4 Ion Beam Sputtering and Thermal Coevaporation

Ion Beam Sputtering and Thermal Coevaporation (also on Inclined Substrates) are particularly suited and cheap for uniform films over large areas. The former appears to be also promising for scaling-up the film production. A European team has deposited YBCO films using coevaporation technique on substrates as large as 20x20cm^2 and reported Jc values of 2x10^{6}A/cm^2 [13].

2.2.5 Chemical non-vacuum techniques

Chemical non-vacuum techniques: Very high J_c values, >3 x 10^6 A/cm^2 have been obtained on Y(123) layers by using *metal organic deposition* and MOCVD. Very recently, high j_c values were also obtained for Spray Pyrolysis, a relatively simple technique with high technical promise [13].

A comparatively simple to deposit large-area thin films rapidly is by MOCVD. The technique depends on the production of volatile metalorganic precursors as sources of the metal elements. Properties required in a suitable precursor include; (a) sufficiently high vapor pressure for vapor transport, (b) stability at operating temperatures without losing volatility, and (c) stability at room temperatures for long term storage [10].

2.3 Present Fabrication Process

In this work, a relatively simple experimental method of film deposition is introduced by dispersion of powder in a liquid medium called suspension, and deposition upon evaporation of liquid. The deposition is employed by placing the substrate in the suspension and evaporating the acetone. This results to evenly distributed film of fine powdered particles on the substrate due to the continual evaporation of the dispersion medium. This is illustrated in Figure 2.6. The complete details of powder deposition are thoroughly discussed in experimental procedures, Chapter Four. The initially loose and porous state of powder deposit will be transformed to oriented crystalline phase by the formation of a liquid phase during partial melting and annealing process.

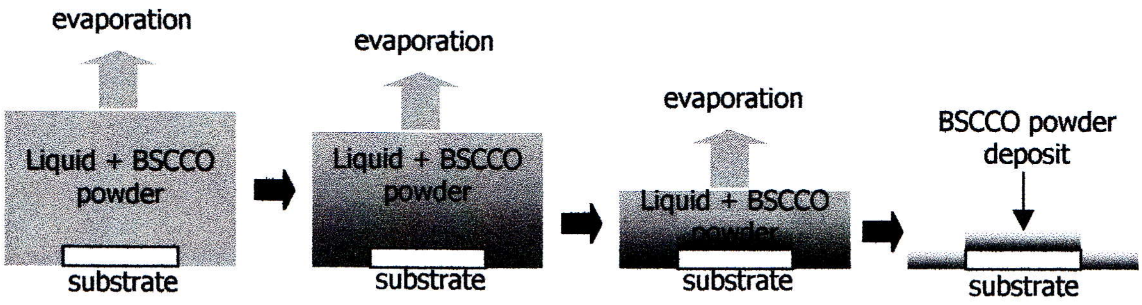
evaporation
Liquid + BSCCO powder
substrate
evaporation
Liquid + BSCCO powder
substrate
evaporation
Liquid + BSCCO powder
substrate
BSCCO powder deposit
substrate

Figure 2.6. *Powder deposition on the substrate by evaporation of the dispersal liquid.*

It will be shown that the present method, which does not involve complicated equipment, yields a perfectly reproducible c-axis oriented superconducting BSCCO thin films that have characteristics comparable to that of grown by other methods.

Reference:

[1] H. Maeda. Y. Tanaka, M. Fukutomi and T. Asano: Jpn. J. Appl. Phys. 27 (1988) L209

[2] M. Takano, J. Takada, K. Oda, H. Kitaguchi, Y. Miura, Y. Ikeda, Y. Tomii and H. Mazaki: Jpn. J. Appl. Phys. 27 (1988) L1041.

[3] A. Oota, A. Kirihigashi, Y. Sasaki and K. Ohba: Jpn. J. Appl. Phys. 27 #12 DEC. (1988) L2289-L2292

[4] V. Garnier, I. Monot-Laffez, G. Desgardin. *Kinetics Study of the Bi-2223 Grain Growth Thickness*. Physica C 349 (2001) 103-112.

[5] P. Majewski, Supercond. Sci. Technol. 10 (1997) 453.

[6] B.R. Lehndorff, *High T_c Superconductors for Magnet and Energy Technology*, STMP. 171, Springer-Verlag Berlin Heidelberg (2001)

[7] P. Majewski, *Materials Aspects of the High-Temperature Superconductors in the System BSCCO*. J. Mater. Res., Vol. 15, No. 4 Apr. 2000

[8] V. Sh. Shekhtman. *The Real Structure of High T_c Superconductors*, Springer-Verlag Berlin Heidelberg 1993 Germany. 1993. p13.

[9] S.H. Pan, E.W. Hudson, J. Ma, and J.C. Davis, *Imaging and Identification of Atomic Planes of Cleaved Bi-2212 by High Resolution Scanning Tunneling Microscopy*. App. Phys. Lett. Vol. 73, No.1, July 1998, 58-60.

[10] A. Bourdillon and N.X. Tan Bourdillon, *High Temperature Superconductors: Processing and Science*. Academic Press, Inc. USA, 1994, pp. 129-130.

[11] K. Kuroda, K. Kojima, K. Yokoyama, and K. Hamanaka, *Effect of Growth Temperature on Superconducting Phases of As-Grown BiSrCaCuO Thin Film Formed by R.F. Magnetron Sputtering*. Jpn. J. Appl. Phys. Vol. 29, No. 11, Nov. 1990, pp. L2033-2036

[12] S. Karimoto, S. Kubo, K. Tsuru and M. Suzuki. *Effects of Substrate Materials on Properties of Superconducting $Bi_2Sr_2CaCu_2O_8$ Epitaxial Thin Films*. Jpn. J. Appl. Phys. 36 (1997) Pt. 1 No. 1A p.85

[13] M. Marezio. *Superconducting Materials*, Material Science and Application

[14] R. Rössler, J.D. Pedaring, Ch. Jooss, *Bi-2212 thin films on c-axis oriented and vicinal substrates*, Physica C, 361 (2001) 13-21

Chapter 3

Powder Characteristics and Liquid Phase Sintering and Annealing Processes

3.1 Powder Characteristics

The mere powder deposition on the surface of the substrate is still not complete to qualify as epitaxially grown film. Grain orientation at deposition is expected to be random and pores are inherent part of it. These pores are present in the powder compact as interparticle voids. In fact, powders do not fill space efficiently. For example, monosized spheres will fill a container to approximately 60% density, and even under vibration will reach a maximum packing density of 64%. Other particle shapes and the application of pressure can give higher densities, but usually there is always porosity between particles. Thus, all powder structures are initially porous. The initial structure is termed the "green" state, reflecting the unfired condition of the powder [1].

In order for the deposited particles to re-orient themselves on the surface substrate and eliminate the pores, microstructural re-arrangement is necessary. This is resolved by employing heat treatment on the deposited film powder via liquid phase sintering process where partial melting occurs in BSCCO material due to incongruent melting. Furthermore, during this process, pore reduction occurs resulting to densification and coarsening of the material.

3.2 Liquid Phase Sintering Process

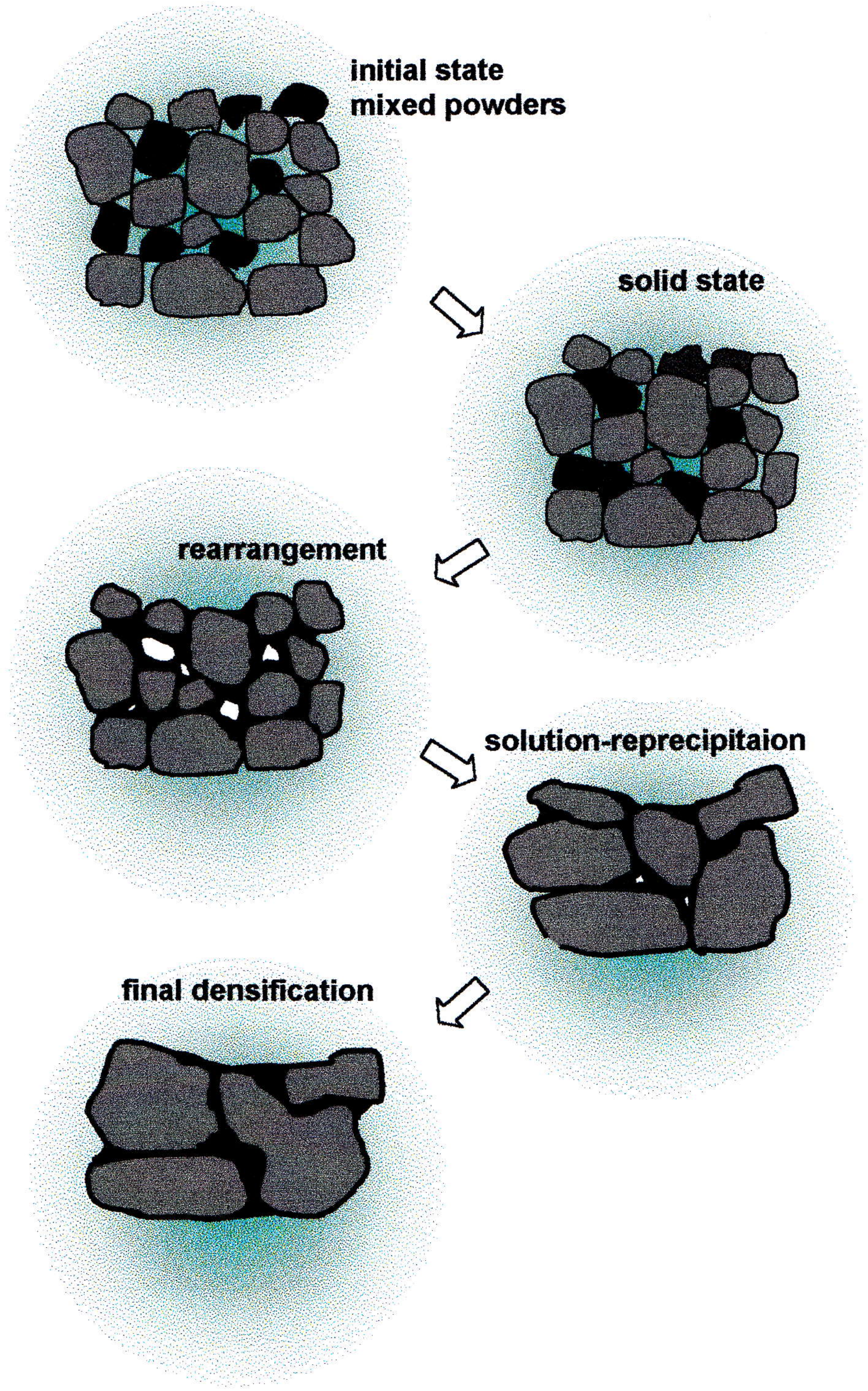
initial state
mixed powders
solid state
rearrangement
solution-reprecipitaion
final densification

Figure 3.1. *Illustration of the classic liquid-phase sintering stages involving mixed powders which form a non-reactive liquid on heating, allowing subsequent particle rearrangement and densification by solution-reprecipitation and solid skeleton sintering.*

The presence of a liquid phase during heat treatment of mixed powders improves and accelerates mass transport rates, densification, and microstructure coarsening. It exerts a capillary pull on the particles that is equivalent to a large external pressure. This reduces the porosity of previously "green" state structure of powder material.

Three major stages in liquid phase sintering process, namely, heating and melting stage, solution-reprecipitation stage, and microstructural coarsening complete the cycle of the sintering process. These major occurrences actually happen in sintering powdered materials and will be adopted as mechanism in the growth of epitaxially oriented BSCCO films. Typical events in these major stages are illustrated in Figure 3.1.

3.2.1 Heating and Melting Stage

Initial stage of liquid phase sintering is the partial melting from the exterior surface. The circumferential shrinkage stresses can lead to component cracking if heating is too rapid. As the melt forms at the surface, capillary stresses will cause the liquid to redistribute itself into the interparticle pores and penetrate the grain boundaries in the particles including formerly formed solid-state sinter bonds between particles. During this period when the liquid forms and spreads, rearrangement events are dominant. The liquid causes particle rearrangement also via capillary forces that results to densification. Liquid redistributes and rearrangement continues until it reaches a relatively stable state.

3.2.2 Solution-Reprecipitation Stage

After the partial melting stage and rearrangement slows down, a process referred to as solution-diffusion-precipitation or simply solution-precipitation becomes dominant.

The solid dissolves at the solid-liquid interfaces with a higher chemical potential, diffuses through the liquid, and precipitates on the particles at the other sites with a lower chemical potential. Usually, the dissolution site is the wetted surface of smaller particles where the smaller particle radius leads to a higher chemical potential. Precipitation then occurs on the surfaces of the larger particle [2]. Grains are pulled into contact by a wetting liquid, allowing coalescence at points of contact. Contacting grains, usually of dissimilar sizes, fuse into a single grain by a continuous process of directional grain growth, grain reshaping, and grain rotation. This process continues until grain size increases while the number of grains decreases [1].

3.2.3 Microstructural Coarsening

In the final stage of the sintering process, coarsening of the microstructure along with densification dominates. This results to further increase in grain size to decrease the interfacial energy at the solid-liquid interface. The microstructural coarsening is accompanied by grain shape accommodation, which allows more efficient packing of grains. Liquid may be released from the more efficiently packed regions, and it may flow into the isolated pores, leading to densification.

Reference:

[1] R. M. German, *Sintering Theory and Practice*, John Wiley & Sons, Inc., Canada, 1996

[2] M.N. Rahaman, *Ceramic Processing and Sintering*, Marcel Dekker, Inc., N.Y. 1995.

Chapter 4
Experimental Procedure

This chapter explains experimental details of epitaxially oriented BSCCO film production by combined method of liquid-assisted deposition technique and subsequent liquid phase sintering and annealing process.

4.1 Film Production

4.1.1 Preparation of Bi-2201, Bi-2212, and Bi-2223 Powder Precursors

The BSCCO powders were first prepared by solid state reaction of the powdered oxides and carbonates of the metals involved with the cations in the required ratios. The ratios have been accurately controlled by weighing the powder precursors in an analytical balance (Sergent-Welch) with accuracy of ±2 mg. The stoichiometric ratios of the powders were based on the following balanced chemical reactions for the synthesis of Bi-2201 (4.1), Bi-2212 (4.2) and Bi-2223 (4.3);

$$Bi_2O_3 + 2SrCO_3 + CuO \rightarrow Bi_2Sr_2CuO_{6+\delta} + 2CO_2 \qquad (4.1)$$

$$Bi_2O_3 + 2SrCO_3 + CaCO_3 + 2CuO \rightarrow Bi_2Sr_2CaCu_2O_{8+\delta} + 3CO_2 \qquad (4.2)$$

$$Bi_2Sr_2CaCu_2O_{8+\delta} + \tfrac{1}{2}Ca_2CuO_3 + \tfrac{1}{2}CuO \rightarrow Bi_2Sr_2Ca_2Cu_3O_{10+\delta} \qquad (4.3)$$

After weighing out the appropriate amounts of Bi_2O_3, $SrCO_3$, $CaCO_3$, and CuO, the chemicals were carefully transferred to an agate mortar and pestle. Using the mortar and pestle, the powder was ground using a twisting circular motion of the pestle. The grinding continues until the resulting mixture is a fine gray powder. To ensure a thorough and homogenous mixture, a protocol of 1 hour grinding per 5 g of powder was followed. The reagents were finely ground and thoroughly mixed, because the multi component phase diagrams usually show competing compounds at nearby compositions. Particle sizes of a few microns are usually required. The mixed powders were then compacted with a uni-axial press and the resulting pellets were placed in an alumina boat ready for initial heat treatment or calcination.

For the calcination process, the alumina boat with the BSCCO pellet sample was placed in a high temperature furnace. Bi-2201, Bi-2212, and Bi-2223 were calcined at soaking temperatures of 810°C, 830°C, and 870°C respectively. The furnace was programmed to heat from room temperature to the soaking temperature for five hours.

The resulting BSCCO powders were then finely ground again until the size is small enough to be in suspension. Acetone was used as the dispersion medium in this work due to its low vaporization temperature and it is readily available in the laboratory.

4.1.2 Film Deposition

The dispersion of the solid particles in liquid acetone was the first step in deposition of the powdered particles on the substrates. The suspension was made by mixing 80 mg of BSCCO powder with approximately 3 mL of acetone. The volume of acetone is arbitrary since it will have to evaporate on purpose later in the experiment. The mixture is then ultrasonicated for fifteen minutes to further disperse the agglomerate particles caused by optimal grinding procedure. Using a flat-bottom container, the MgO single crystal substrate was placed lying at the bottom. The resulting slurry was then poured in the container containing the MgO substrate. The bottom area of the container is 240.53 mm^2. The powder weight was fixed to 80 mg, so that the deposited powder on the substrate is fixed to 0.33 mg/mm^2. An actual sequential picture of deposition procedure is shown in Figures 4.1 and 4.2.

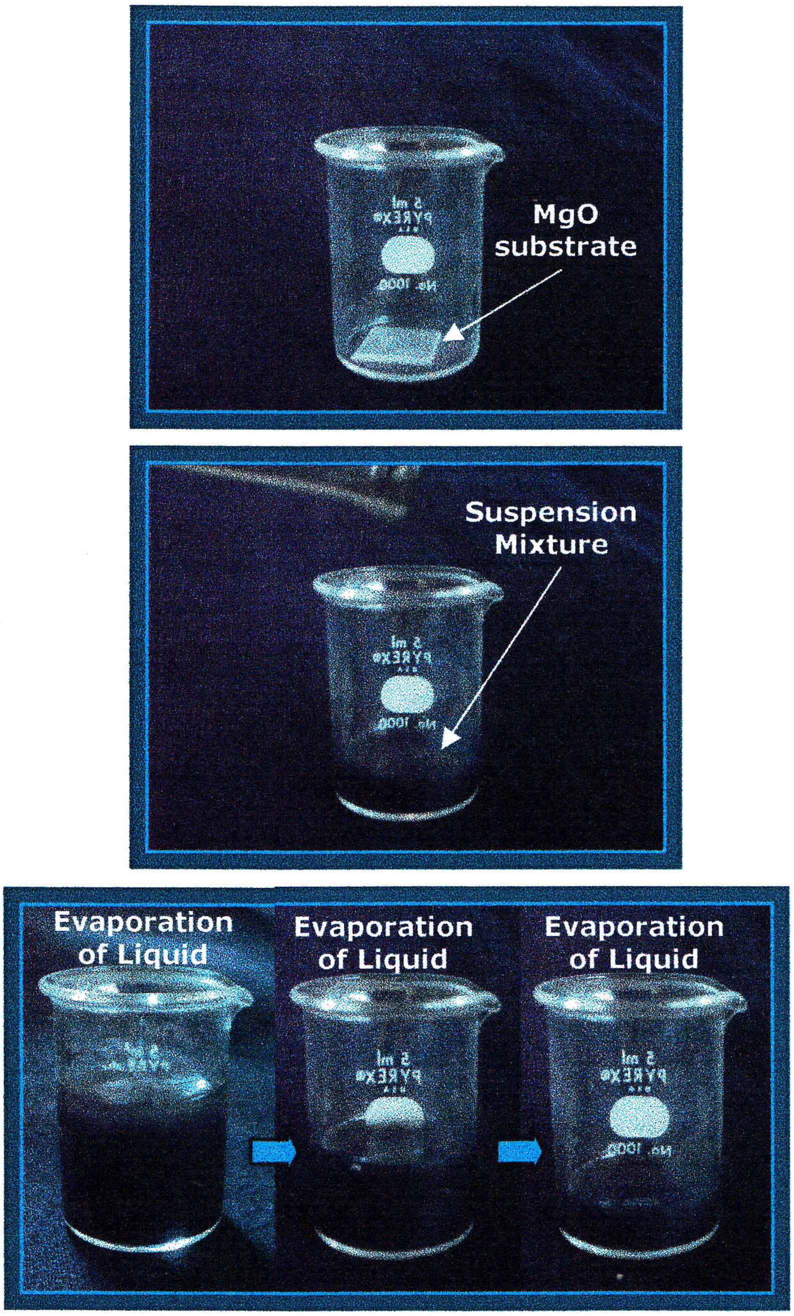
MgO substrate
Suspension Mixture
Evaporation of Liquid
Evaporation of Liquid
Evaporation of Liquid

Figure 4.1. *Sequential procedure of powder deposition on MgO through the evaporation of liquid dispersant, acetone.*

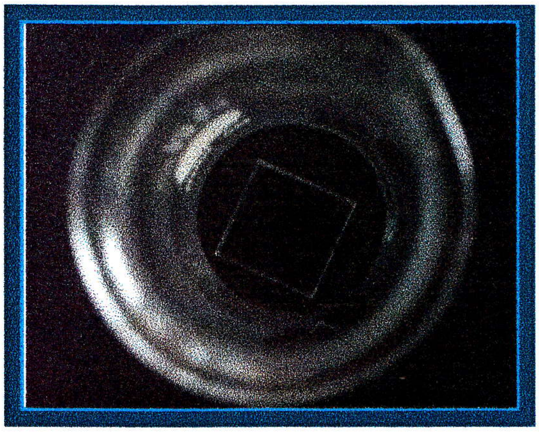

Figure 4.2. *After evaporation of acetone, what is left is the evenly deposited powder on the surface of MgO substrate.*

The deposited powder is expected to be initially loose after the evaporation of acetone so careful handling is observed whenever the film is transported. It is also important to clean the edges of the substrate to be free from deposited powder because it may cause a capillary action that results to transport of BSCCO material underneath the substrate during the sintering process.

4.1.3 Film Heat Processing and Annealing

In order to achieve the high *c*-axis alignment of the initially porous powdered film, the process of crystal growth and alignment of grains have to be accomplished through application of heat where microstructural changes happen. The formation of epitaxial BSCCO film is achieved by liquid phase sintering and annealing technique. This can be accomplished by heat treatment of the material slightly above the incongruent melting where the BSCCO partially melts. The presence of liquid phase helps in densification, removal of pores, and coarsening of the material to produce the film. After the partial melting of the material, film annealing is done where subsequent isothermal treatment for several hours is employed. This is usually at a lowered temperature to reform and facilitate the growth of BSCCO film. A general temperature profile is shown in figure 4.3. The melting temperature used for all the samples is 950 ^oC for 1 hour. At that temperature, a liquid phase is present based on the equilibrium phase diagram of Figure 2.2.

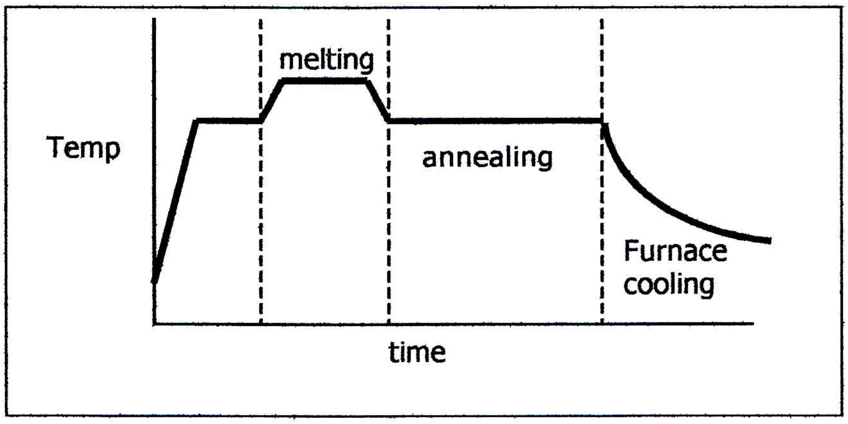

Figure 4.3. *Heat treatment temperature profile.*

4.2 Film Characterization

4.2.1 X-Ray Diffraction

X-Ray diffraction made it possible for the identification of the fine structure of matter from the time of its discovery by a German physicist von Laue in 1912. It was used initially for the determination of crystal structure but later on developed to apply to such diverse problems such as chemical analysis and stress measurement, to the study of phase equilibria and the measurement of particle size, and to the determination of the orientation of one crystal or the ensemble of orientations in a polycrystalline aggregate [1].

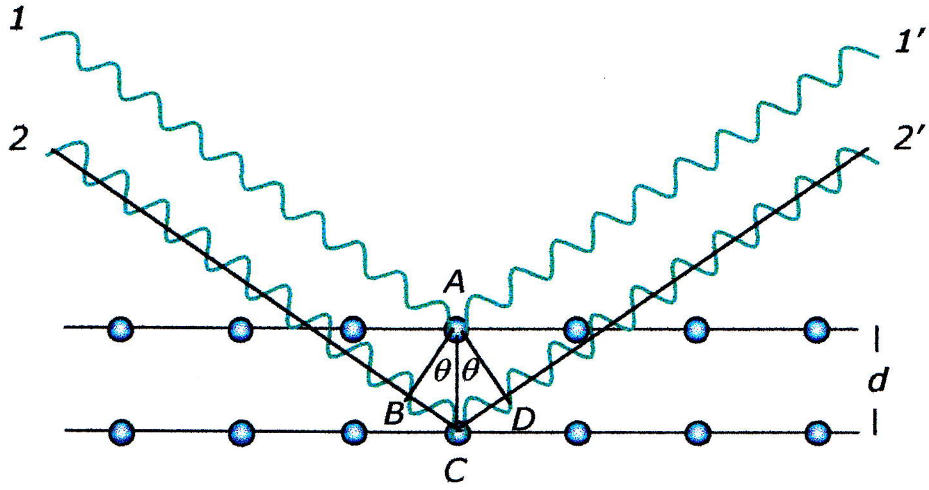

Figure 4.4. *Diffraction of x-rays by a crystal.*

Consider the two lattice planes in Figure 4.4. Assuming that the beam is perfectly parallel, perfectly monochromatic x-rays of wavelength λ is incident on this crystal at an angle θ, called the Bragg angle. Rays 1 and 2 for example, are scattered by atoms *A* and *C* respectively, and the path difference between *1-A-1′* and *2-C-2′* is;

$$BC + CD = d\sin\theta + d\sin\theta \tag{4.4}$$

Scattered rays 1′ and 2′ will be completely in phase if this path difference is equal to a whole number *n* of wavelengths, or if;

$$n\lambda = 2d\sin\theta \tag{4.5}$$

where *n* is called the order of reflection where it may take on any integral value consistent with sin θ not exceeding unity and is equal to the number of wavelengths in the path difference between rays scattered by adjacent planes. This relation is known as the Bragg law, formulated by W.L. Bragg. It states the essential condition, which must be met if diffraction is to occur.

In XRD characterization of the film, Bede 3D High Resolution X-Ray Diffractometer was used using copper target as the x-ray source. The sample was mounted such that the surface plane of the film is considered as the reflecting plane. In this orientation, if the *c*-axis of the BSCCO film is oriented perpendicular to the surface plane of the substrate, only the reflecting planes with Miller indices ($0\ 0\ \ell$) will conform to the Bragg condition for the diffraction to occur. A simulation of XRD scan of *c*-axis oriented BSCCO and MgO (001) single crystal substrate are shown in Appendix A.

4.2.2 Scanning Electron Microscopy

Scanning Electron Microscope (SEM) is one of the most versatile instrument available for the examination and analysis of the microstructural characteristics of solid objects. The signal commonly used in SEM imaging for surface morphology investigations is the secondary electron signal. The secondary electrons are of low energy, 0-10eV, emitted from the surface of a specimen, scanned by the focused electron beam accelerated by a potential between 5 and 40 kV. The secondary electron image is often affected by artifacts on the specimen surface, including surface corrosion and surface topography, especially on fractured specimens. This is because the secondary electrons exit from a shallow depth owing to their low energies. They are therefore sensitive to surface phenomena, and secondary electron images provide comparatively high spatial resolution because most emission originates close to the point of incidence of the focused probe. The secondary electron coefficient is of particular value in examining high T_c systems because most second phases are insulating. Since the high T_c superconductors are metallic, it is not necessary to coat the specimens with conducting films [2]. JEOL JSM-5310 scanning microscope was used in the investigation of the surface morphology of the film samples.

4.2.3 Resistivity Measurements: The Four-Probe Technique

A four-probe technique arrangement is utilized for the zero-resistance characteristic of BSCCO superconductors and is shown schematically in Figure 4.5. The illustration shows the schematic diagram of four probes connected to the film and the temperature is measured by a temperature sensor in thermal contact with the film. Electrical contacts used on the film were pressed indium solder and connected to the sample mount with gold wires. Contacts should be ohmic and of low resistance since it is important not only to characterization, but also to device fabrication. In both bulk and thin film applications, the interface between the metal and superconductor is critical [2].

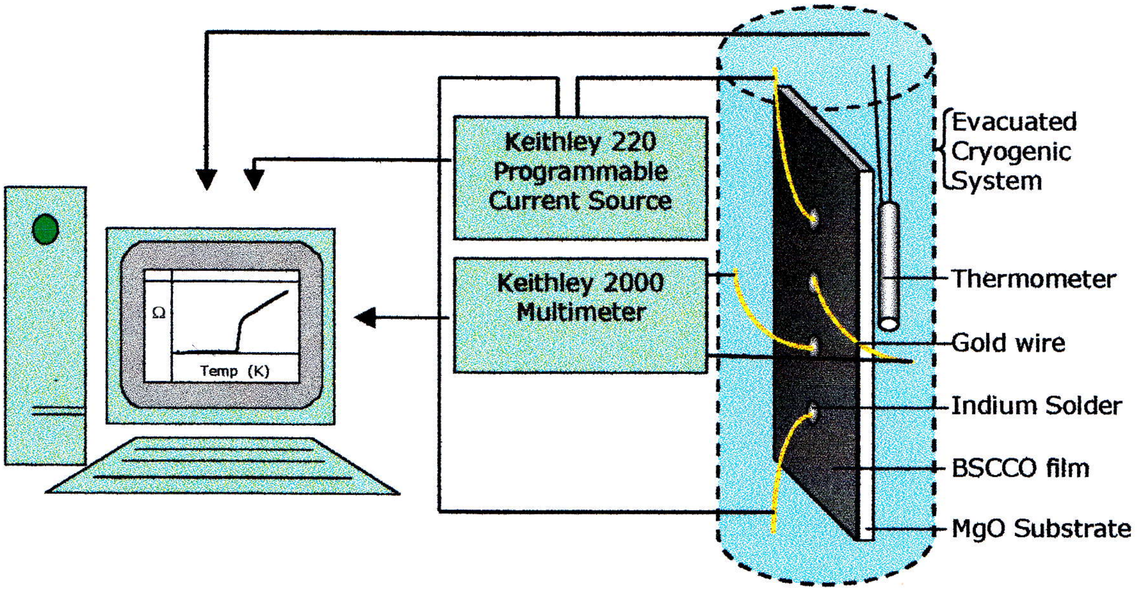
Keithley 220
Programmable
Current Source
Keithley 2000
Multimeter
Ω
Temp (K)
Evacuated
Cryogenic
System
Thermometer
Gold wire
Indium Solder
BSCCO film
MgO Substrate

Figure 4.5. *Illustration of simple cryogenic system for four-probe measurement.*

A dc resistivity of the superconducting film was measured by the voltage drop (Keithley 2000 multimeter) across the film when a current of known magnitude passes (Keithley 220 programmable current source).

Reference:

[1] B.D. Culllity, *Elements of X-Ray Diffraction*.

[2] A. Bourdillon and N.X. Tan Bourdillon, *High Temperature Superconductors: Processing and Science*. Academic Press, Inc. USA, 1994, pp. 129-130.

Chapter 5
Results and Discussions

5.1 Scanning Electron Microscopy Analysis

5.1.1 Initial Deposited Powder Characteristics

In order to analyze the effect of annealing on the deposited powder, attention must be paid first to the initial powder characteristics prior to annealing. Important powder characteristics such as grain size, size distribution, shape and state of agglomeration must be observed. Figure 5.1 shows the SEM image of the initial powder, prior to suspension and deposition. It is assumed that after powder deposition on the

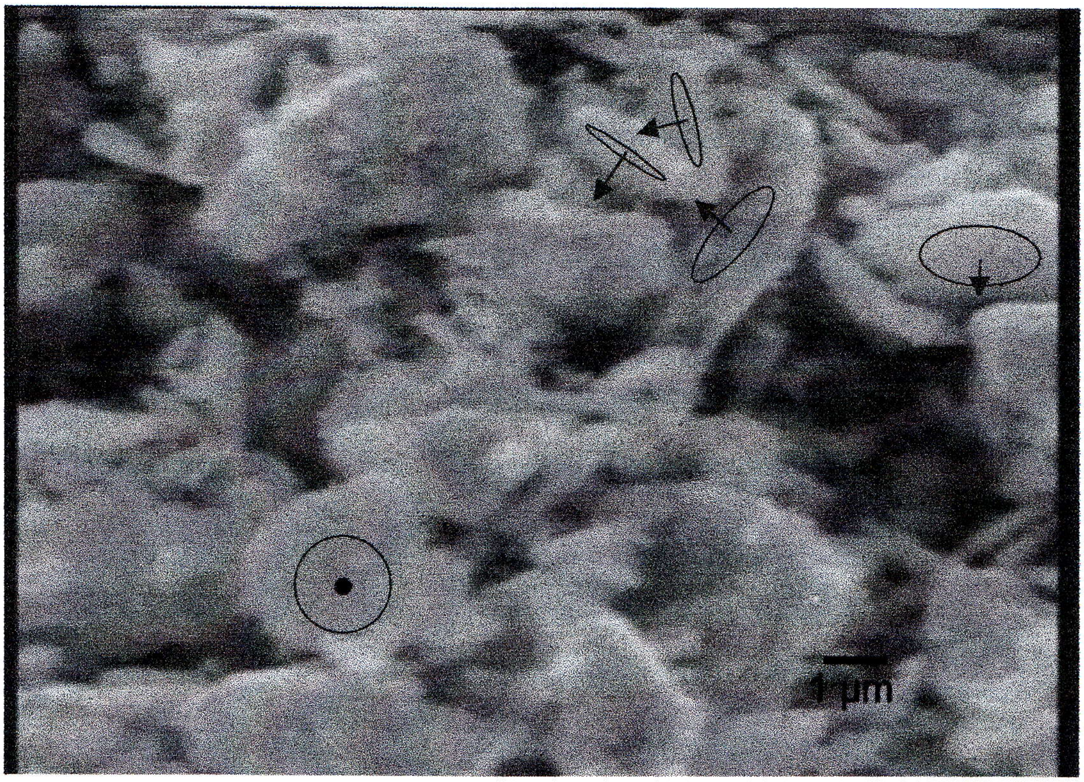

Figure 5.1. *Scanning electron micrograph of initial BSCCO powder. Sizes range from some fraction of a micron to around 4 microns plate-like grains. Arrows indicate the c-lattice direction of the grains.*

substrate material, the powder state is most likely the same state as Figure 5.1 or probably much denser powder compaction due to evaporation of acetone. It can be seen that the size varies ranging from around a fraction of micron to as much as 4 microns of platelet-like grains and some irregular-shaped grains. The plate-like, or sometimes sheet-like growth habit is a characteristic of a single crystalline BSCCO material, with *c*-axis along the thickness of the plate. Those irregularly-shaped grains are formed due to mechanical grinding preparations. SEM shows that the *c*-axis direction of plate-like grains is random and grains are distributed all over. The randomness of the grains will be used as the initial basis in establishing the mechanism of epitaxial alignment during heat treatment, resulting to *c*-axis oriented BSCCO films.

5.1.2 The Films After Liquid Phase Sintering and Annealing Process

After the deposited powder on MgO underwent liquid phase sintering and annealing processes, the grains and porosity that were initially observed became undistinguishable. The deposited powder layer resulted to a flat layer of film on the surface of single crystalline MgO substrate. SEM image of the film in Figure 5.2a shows no sign of granularity and absence of pores. The relatively smooth surface film obtained can be compared with that of grown by pulsed laser deposition done by the group of R. Rössler et.al. (Figure 5.2b). However, presence of some steps and layering can be observed to be distributed on some parts of the surface of the films grown by the present method (Figure 5.2c). The presence of these pronounced layered structures seen in Figure 5.2c is due to the significantly different parameters of the *a,b* axis and *c* axis. The crystallization rate in the direction of the *a,b* plane is about 1000 times faster than the *c* direction. This exhibits the mica-like or sheet-like microstructure layering resulting to a pronounced cleavability parallel to the *a,b* plane due to the weak bonding between the neighboring BiO layers [6]. Figure 5.2d shows this sheet-like structure for a Bi-2223 single crystal presented by P. Majewski.

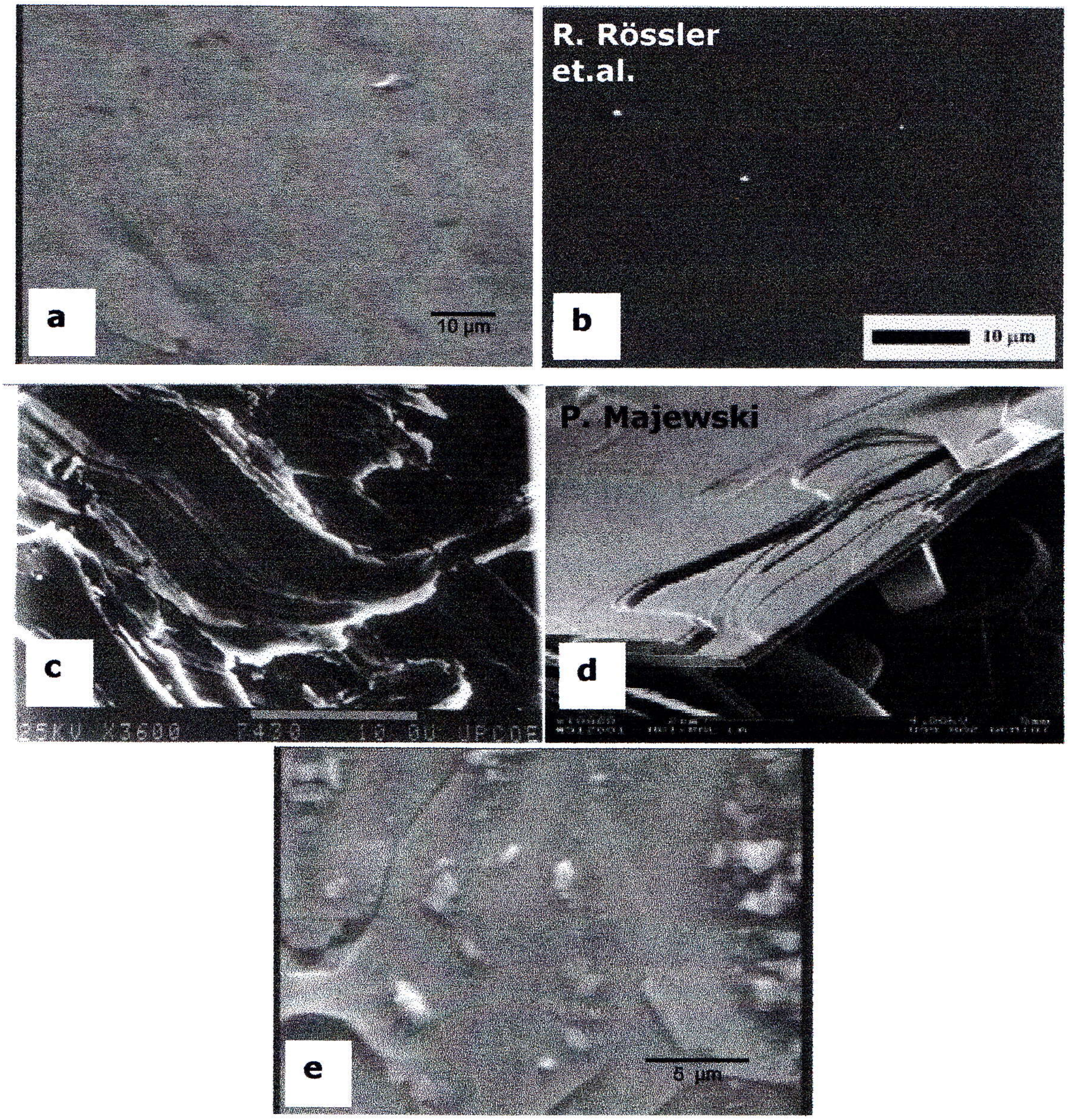
R. Rössler
et.al.
a
10 µm
b
10 µm
c
25KV X3600
10.0U
P. Majewski
d
e
5 µm

Figure 5.2. *Microstructures of SEM images of film; a) smooth surface, b) smooth surface obtained by PLD (R. Rössel, et. al), c) layered structure characteristic of BSCCO, d) layered structure of BSCCO single crystal (P. Majewski), e) Granularity and presence of impurity precipitates in multi-phase BSCCO.*

The features of the films discussed above were observed in all Bi-2201, Bi-2212 and the multi-phase (Bi-2212)-(Bi-2223) films annealed at their optimum temperatures. The multi-phase film however has higher density of impurity precipitates. Note these precipitates shown in Figure 5.2e. These impurity precipitates are the excess products for the formation of Bi-2212 from stoichiometric Bi-2223 precursors, such as the excess calcium and copper compounds. Also, observe the apparent grain boundary, which caused by the partial melting of the powder during the liquid phase annealing process. The film thickness, *t*, was measured to be about 13 μm, as shown in figure 5.3.

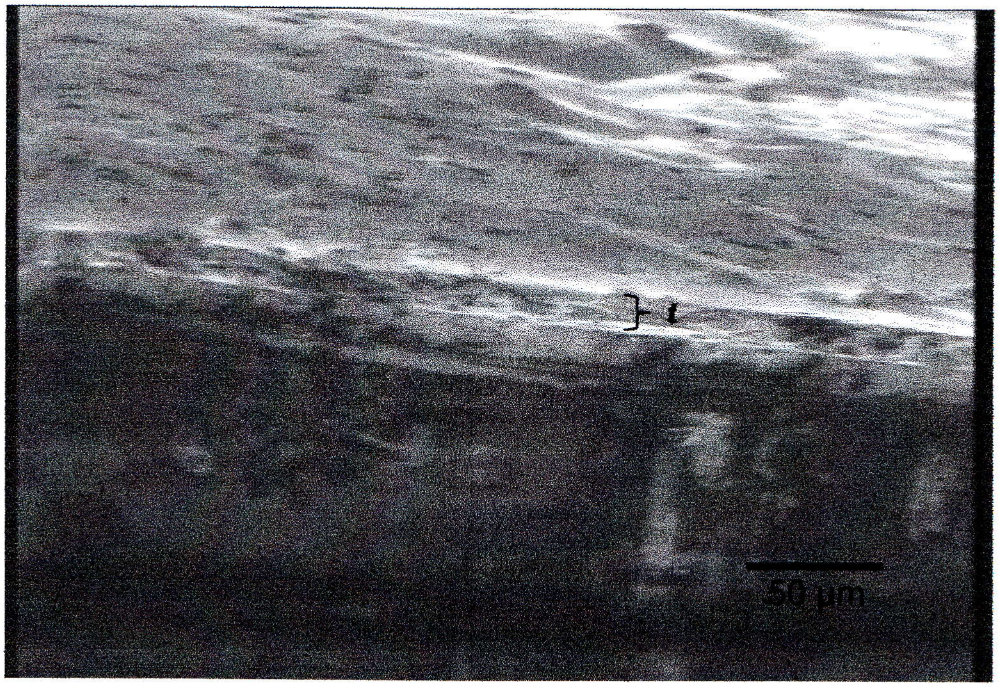

Figure 5.3. *SEM image of the film showing the thickness, t, of about 13 μm.*

5.2 X-Ray Diffraction Analysis

5.2.1 Film Orientation and *c*-Lattice Parameter Determination

To confirm the *c*-axis orientation of the grown films and to determine the phases present, X-Ray Diffraction method was utilized. Moreover, the *c*-lattice parameter was calculated to further verify the BSCCO material. The following X-Ray Diffraction analyses imply that, after the heating treatment, the initially randomly oriented grains at deposition have re-oriented to produce an epitaxially grown film with *c*-axis orientation perpendicular to the surface of MgO substrate. This proves the feasibility of obtaining an epitaxial BSCCO film by the use of the method being presented. To simplify the analyses, the discussions are divided into three according to the three phases in the BSCCO system, the Bi-2201, Bi-2212, and Bi-2223.

5.2.1.1 XRD analysis of the $Bi_2Sr_2CuO_{6+\delta}$ (Bi-2201) film

The XRD scan of Bi-2201 film is shown in Figure 5.4. The indexed peaks pertaining to the Bi-2201 phase show (00ℓ) Miller indices where ℓ= 2,6,8,10,12, 14, and 16. This confirms that the grown film is oriented along the *c*-axis, perpendicular to the surface of the substrate. An XRD simulation of *c*-axis oriented Bi-2201 film is shown in Appendix A. So as not to complicate matters, other peaks have been initially marked with dots. It will be established later, in section 5.2.2, that these peaks also belong to the *c*-axis Bi-2201. Other peaks are impurity phases marked with squares.

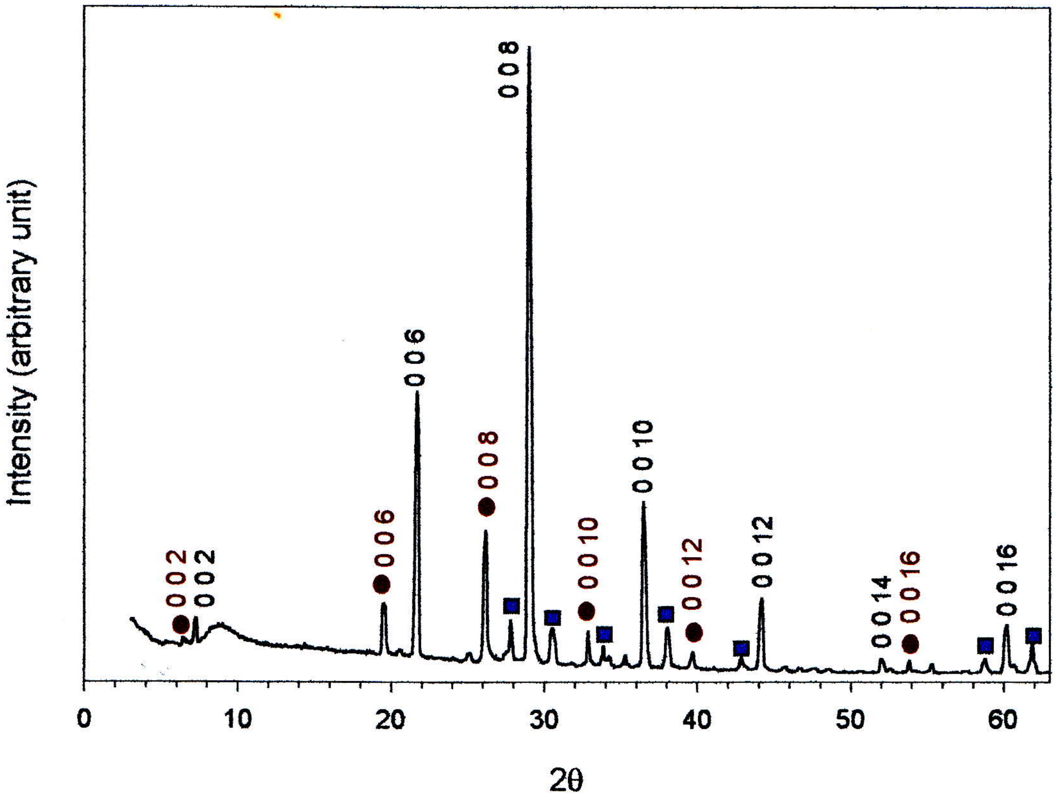

Figure 5.4. *X-ray diffraction scan of Bi-2201 film.*

To calculate for the *c*-lattice parameter of the Bi-2201 and to further confirm the correctness of the peak assignments, the method of least squares was utilized. This was done by plotting ℓ values vs. $\frac{1}{d}$, where *d* is the lattice spacing calculated from the Bragg equation (4.5);

$$\frac{1}{d} = \frac{2\sin\theta}{\lambda} \tag{5.1}$$

The wavelength, λ, of the CuKα_1 radiation used in the experiment is given as, $\lambda = 1.54$ Å. The plot of ℓ vs. $\frac{1}{d}$ is shown in Figure 5.5.

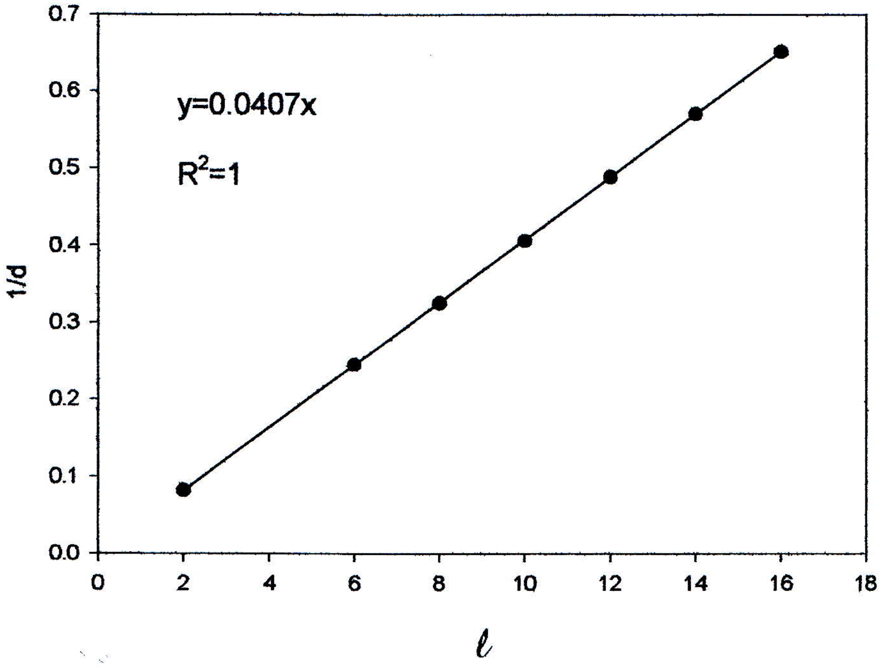

Figure 5.5. *Plot of ℓ vs.* $\frac{1}{d}$. *The slope is equal to* $\frac{1}{c}$ *which resulted to c-lattice parameter to 24.6 Å.*

The calculation of *c*-lattice parameter for Bi-2201 was done using the equation of *d* spacing for orthorhombic lattice[1];

$$\frac{1}{d^2}=\frac{h^2}{a^2}+\frac{k^2}{b^2}+\frac{\ell^2}{c^2} \tag{5.2}$$

The Bi-2201 actually has orthorhombic lattice geometry but is nearly tetragonal (pseudo-orthorhombic), thus, the general equation of orthorhombic was used. The (00ℓ) values of the Miller indices from the XRD data set the h and k values of equation (5.2) to zero resulting to;

$$\frac{1}{d}=\frac{\ell}{c} \tag{5.3}$$

Equation (5.3) forms a general equation of a line, $y = mx + b$, where $y = \frac{1}{d}$, $m = \frac{1}{c}$, and b=0. The *c*-lattice parameter can now be calculated from the slope of Figure 5.5 and is equal to *c*=24.57 Å. This is the *c*-lattice parameter for Bi-2201. The R-squared value, which is equal to unity, further confirms that the peak assignments for the Bi-2201 are correct.

5.2.1.2 XRD analysis of the $Bi_2Sr_2CaCu_2O_{8+\delta}$ (Bi-2212) film

Similar analysis was also done in the case of Bi-2212 film. The XRD scan of Bi-2212 film is shown in Figure 5.6. The XRD scan also confirms the *c*-axis orientation of

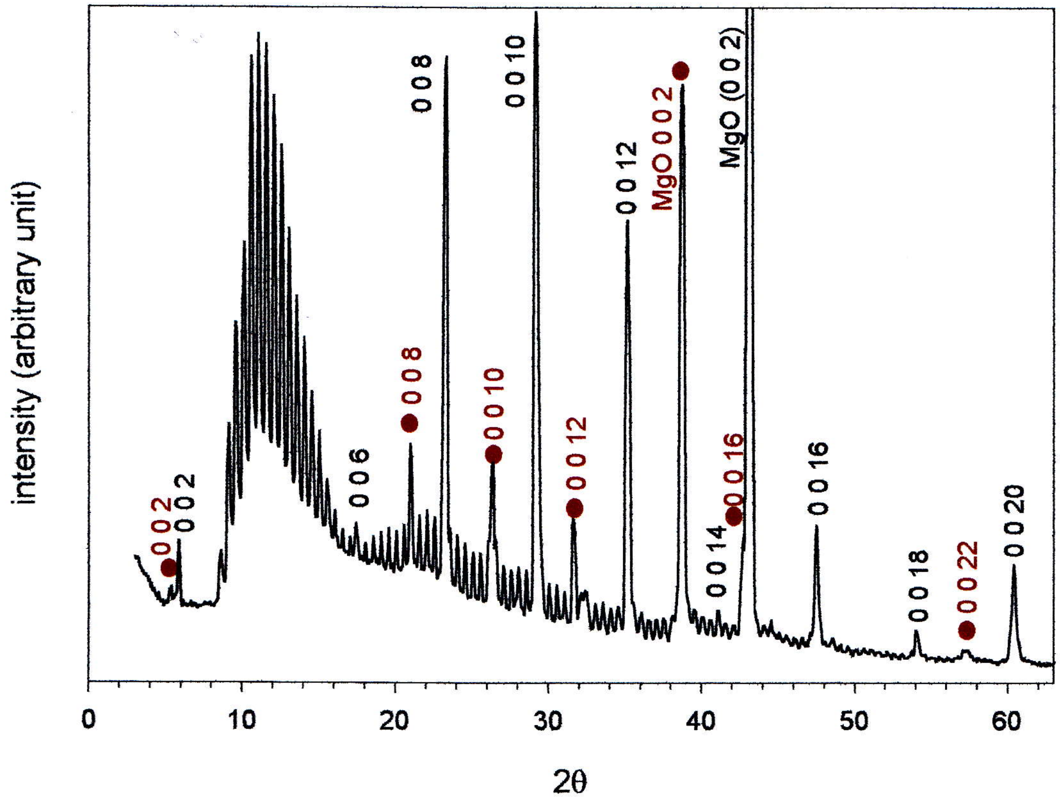

Figure 5.6. *X-Ray Diffraction Scan of Bi-2212 film.*

the film. The Miller indices show only the (00ℓ) diffraction peaks for Bi2212 where ℓ=2, 6, 8, 10, 12, 14, 16, 18, and 20. An XRD simulation of *c*-axis Bi-2212 film is shown in Appendix A. Note also the presence of other peaks marked with dots. Brehmsstrahlung background can also be seen creating the base of the peaks. Also observed is the constant oscillation of the background significantly evident from 2θ=10° to 30°. At film interfaces, the electron density changes so the refractive index also changes causing some x-rays to be reflected to the interfaces. Since a film has a top and bottom interface, interference between x-rays reflected at these interfaces leads to this oscillatory pattern [3]. These oscillations are called the Kiessig fringes that indicate good layering of the film on the surface of MgO substrate. These fringes also indicate that the layer thickness is uniform and interface roughness is small [4,5].

The calculation of *c*-lattice parameter was also done in the same manner discussed in the previous section. Figure 5.7 shows the plot of ℓ vs. $\frac{1}{d}$, where the slope,

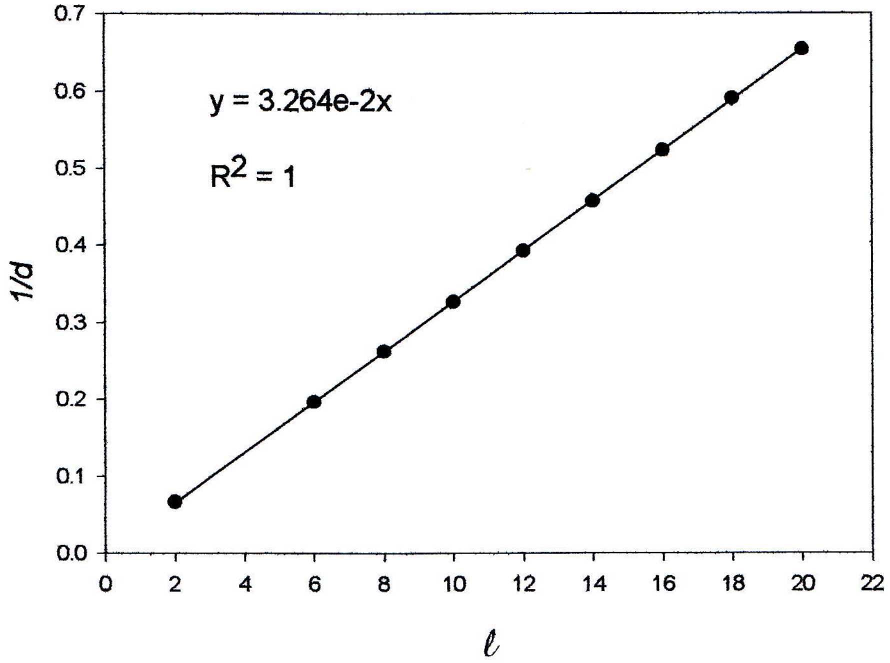

Figure 5.7. *Plot of ℓ vs. $\frac{1}{d}$. The slope is equal to $\frac{1}{c}$ which resulted to c-lattice parameter to 30.6 Å.*

m, is equal to $\frac{1}{c}$, *c* is the lattice parameter. This resulted to *c*=30.6 Å, which corresponds to the *c*-lattice parameter for Bi-2212. The *c*-lattice parameter and the R-squared value to unity again suggest the correct assignment of peaks for the Bi-2212 film.

5.2.1.3 Multi-phase, $Bi_2Sr_2CaCu_2O_{8+\delta}$ (Bi-2212) and $Bi_2Sr_2Ca_2Cu_3O_{10+\delta}$ (Bi-2223), film

For the stoichiometric Bi-2223 precursors, equation (4.3), the film sample has multi-phase growth, as expected, due to the difficulty of Bi-2223 single-phase synthesis. Figure 5.8 shows the XRD scan of the sample where the intensity peaks are

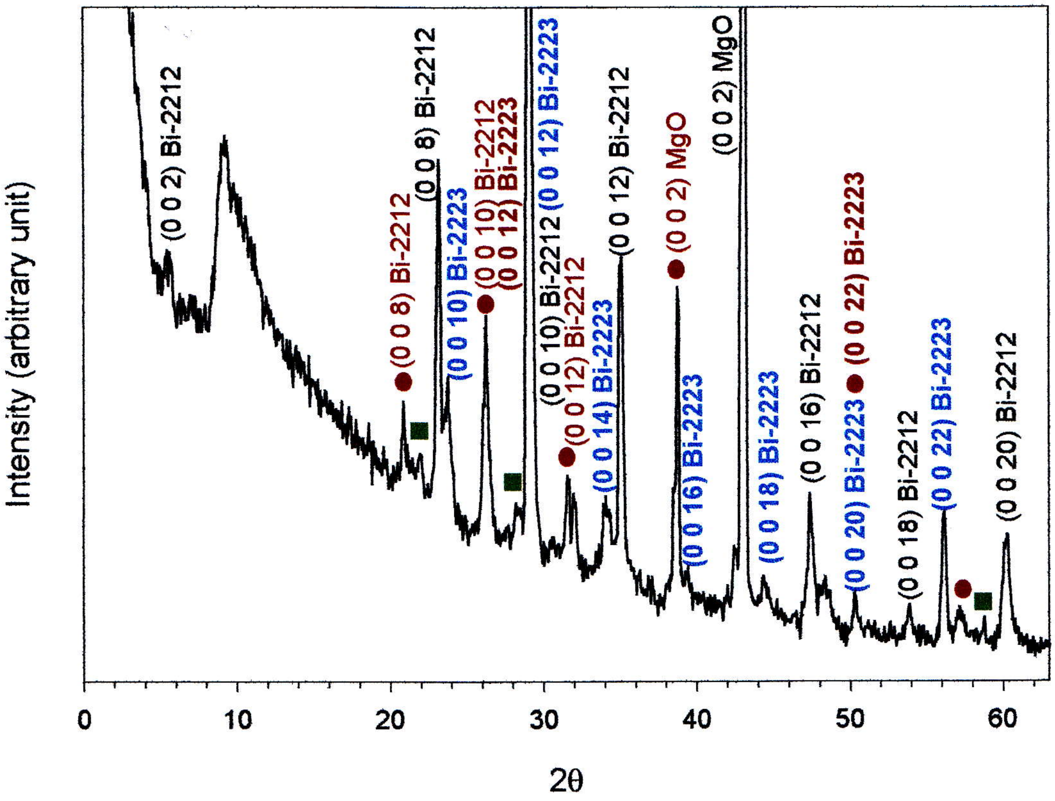

Figure 5.8. *X-Ray Diffraction Scan of Bi-2223 film.*

superposition of the individual reflection of planes from Bi-2212 and Bi-2223 phases. The dominant phase is the Bi-2212 since its relative intensity peaks are much greater than the peak intensities due to the Bi-2223 phase. Notice that both the Bi-2212 and Bi-2223 phases exhibit *c*-axis orientation as can be observed with the (00ℓ) diffraction indices. The ℓ values are indicated as ℓ = 2, 8, 10, 12, 16, 18, 20 and ℓ = 10, 12, 14, 16, 18, 20, 22 for Bi-2212 and Bi-2223 respectively. The peaks marked with squares are impurity phases. An XRD simulation of *c*-axis oriented Bi-2223 and Bi-2212 are shown in Appendix A.

Figure 5.9 shows the plot of plot of ℓ vs. $\frac{1}{d}$, for the calculation of the *c*-lattice parameters of both Bi-2212 and Bi-2223 phases. The slopes are $m_{\text{Bi-2212}}=0.0326$ and $m_{\text{Bi-2223}}=0.0274$ which corresponds to $c_{\text{Bi-2212}}=30.7$ Å and $c_{\text{Bi-2223}}=36.6$ Å. The R-squared

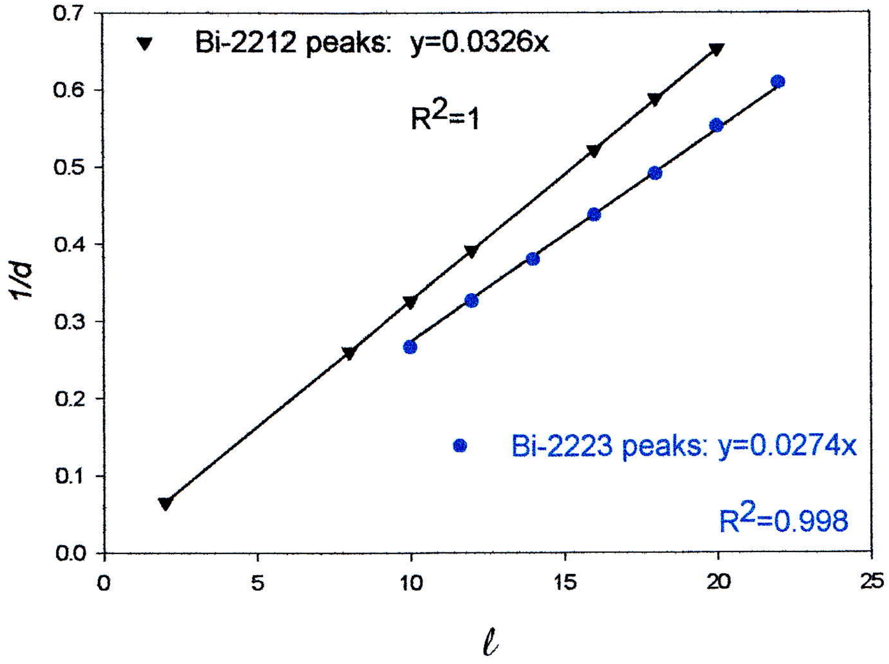

Figure 5.9. *Plot of ℓ vs. $\frac{1}{d}$ for the multi-phase sample. The slope is equal to $\frac{1}{c}$ which resulted to c-lattice parameter to 30.7 Å for Bi-2212 and 36.6 Å for Bi-2223.*

value of the Bi-2212 is equal to unity, thus, the peak assignments are correct. However in the case of Bi-2223 peaks, the R-squared value is slightly not equal to unity due to low intensity and broadness of the peaks. Still, the peaks indices are correct because the calculated *c*-lattice parameter corresponds to the Bi-2223 phase.

The slight variations of the *c*-lattice value, which is attributed to the deviation in the peak positions, may be attributed to phase intergrowth introducing stacking faults and structural modification along the film *c*-axis and non-optimized oxygen stoichiometry [2].

5.2.2 Extraneous X-Ray Peaks

The x-ray peaks marked with dots in previous discussions are somehow misleading in interpreting an x-ray diffraction data. One can be deceived by the peaks

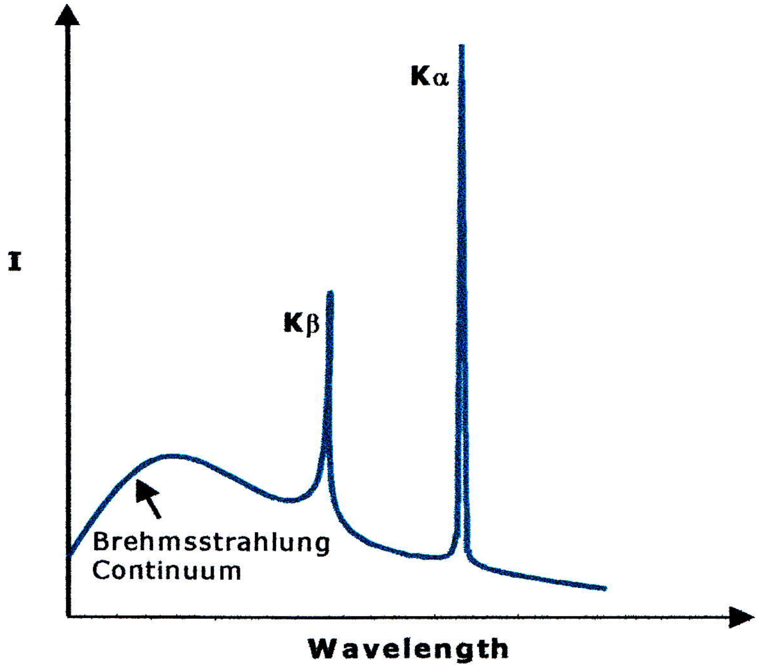

Figure 5.10. *Spectrum of Cu radiation containing the Kα and Kβ X-Ray lines with wavelengths of 1.54051 and 1.39217 angstrom respectively.*

as diffractions coming from phases other than the BSCCO materials. These peaks, marked with dots, were actually extraneous peaks resulting from the Kβ line of the x-ray spectra coming from the copper radiation. Figure 5.10 shows the typical x-ray spectra of copper radiation. The spectra from an x-ray tube contain not only the strong *K*α line but also the weaker *K*β line and the continuous spectrum commonly known as the Brehmsstrahlung radiation that forms the base of the two sharp peaks. The characteristics x-ray lines of *K*α and *K*β have wavelengths of 1.54051 and 1.39217 angstrom respectively.

To show that the dotted peaks are due to the *K*β line of the Cu radiation, let $\theta_{K\alpha}$ be the peak positions due to the *K*α line with wavelength $\lambda_{K\alpha}=1.54051$, and let $\theta_{K\beta}$ be the peak position due to *K*β line with wavelength $\lambda_{K\beta}=1.39217$. The resulting Bragg equations are;

$$2d\sin\theta_{K\alpha} = \lambda_{K\alpha} \tag{5.4}$$

$$2d\sin\theta_{K\beta} = \lambda_{K\beta} \tag{5.5}$$

where *d* is the lattice spacing. Combining equations (5.4) and (5.5) will result to the relations between the peak position due to *K*β and *K*α lines;

$$\sin\theta_{K\beta} = \frac{\lambda_{K\beta}}{\lambda_{K\alpha}}\sin\theta_{K\alpha} \tag{5.6}$$

The ratio $\frac{\lambda_{K\beta}}{\lambda_{K\alpha}}$ is constant and is equal to 0.9037.

Plotting the sine of the peak positions due to *K*β line vs. sine of the peak positions due to *K*α line gives a slope of a constant value, 0.903, as shown in figure 5.11. This confirms the existence of extraneous peaks, which are really attributed to the *K*β line of the Cu radiation.

In essence, the XRD data in Bi-2201 film shows a major phase of Bi-2201 and some minor impurities. The dotted peaks pertain to the same *c*-axis oriented Bi-2201 material present in the sample. For the Bi-2212 film, it shows that the film is a pure phase Bi-2212 material and no other phases were detected. The dotted peaks also pertain to the *c*-axis Bi-2212 material. For the multi-phase film sample, there are only two phases present. A significant amount of the *c*-axis oriented Bi-2212 material and few of the *c*-axis oriented Bi-2223 material.

One way to attenuate the undesirable extraneous peaks is by passing the beam through a filter made of a material whose K absorption edges lies between the $K\alpha$ and $K\beta$ wavelengths of the target metal. Such material will have an atomic number 1 or 2 less than that of the target metal such as nickel [1]. Apparently, nickel filter had not been used during the XRD experiments.

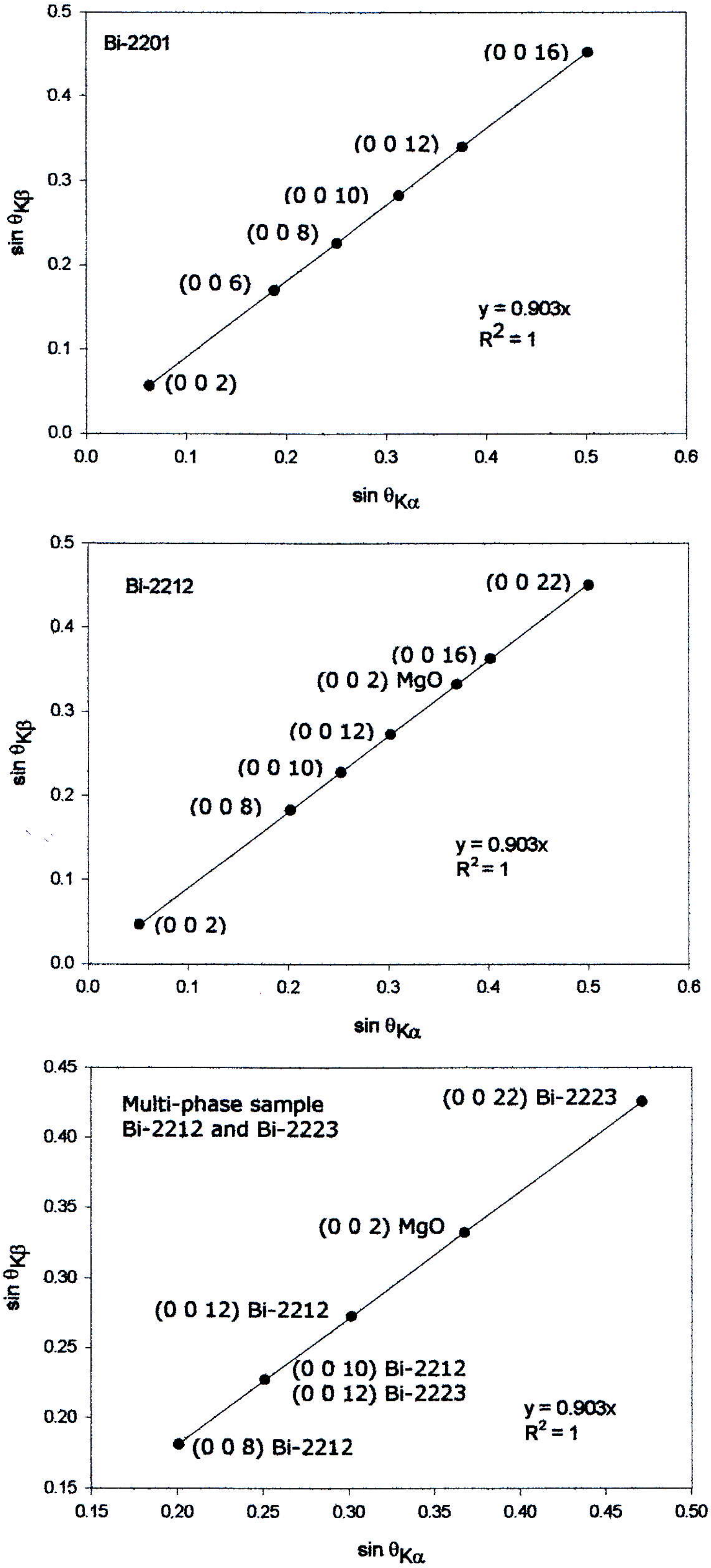

Figure 5.11. *Peak relations due to the Kβ and Kα lines obtained from the experimental XRD data. All results to constant slope of 0.903 which is comparable to the ratio constant,* $\frac{\lambda_\beta}{\lambda_\alpha}$*, of equation (5.6).*

5.2.3 BSCCO Relative Phases Determination

It should be noted that the amount of phases from the following calculations are purely an approximation. The observed intensities from the XRD data may depart from the theoretical values due to certain effects, which can cause great difficulty in quantitative analysis. One of the factors is the preferred orientation of the film grown. In quantitative analysis of the diffraction pattern from XRD data, it is required that the orientation of the constituent crystal is random. Another factor is the presence of other characteristic X-Ray such as the CuKβ and the continuous radiation or the bremstrahlung background. Radiation due to Kβ causes extraneous diffraction peaks that may overlap with the diffraction peak of the Kα line, while the background radiation causes some peaks to be almost invisible in relation to the background. XRD simulations are shown in Appendix A.

Assuming such factors, the relative phase amount of the film with other BSCCO phases can now be approximated. For the Bi-2201 and Bi-2212 film samples, since there are no other peaks of the BSCCO phases, the samples are relatively pure phases. For the multi-phase sample, the relative amount of each phases can be calculated by Gaussian fitting of the (0 0 8) reflection for Bi-2212 and (0 0 10) reflection for Bi-2223. These two reflecting planes are chosen since there are no interfering peaks. Also lower angle is preferable when comparing relative intensity value. The amount of each phases relative to other phases can be calculated from the area of the Gaussian curve shown in Figure 5.12. Summarized in Table 5.1 are the relative phases amount of the film samples with respect to other BSCCO phases.

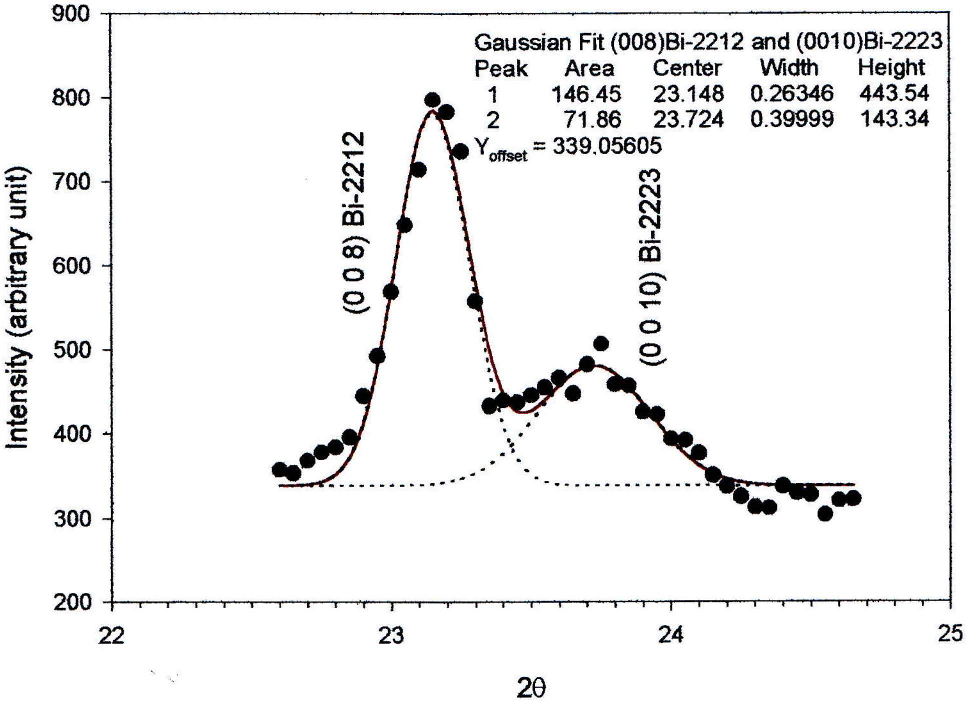

Figure 5.12. *Gaussian fitting of the (0 0 8) reflection for the Bi-2212 and (0 0 10) reflection for the Bi-2223.*

Table 5.1. *Relative amount of BSCCO phases of film samples.*

	Relative to BSCCO phases
Bi-2201	100%
Bi-2212	100%
Multi-phase Bi-2212 and Bi-2223	66% Bi-2212 / 33% Bi-2223

5.3 Superconducting Characteristics

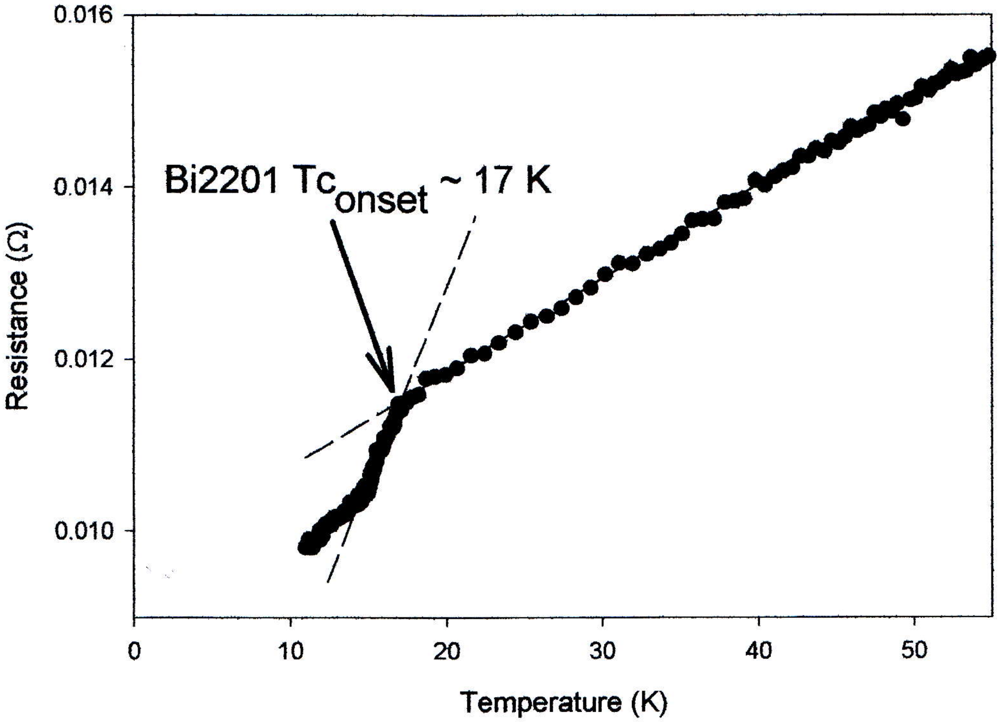

Figure 5.13. *Temperature dependence of resistance of Bi-2201 film. The critical temperature is around 17 K.*

The superconducting property of the BSCCO films was confirmed by the temperature dependence of its resistance. Figure 5.13 shows the resistance curve as a function of temperature for the Bi-2201 film sample. The normal resistance shows a metallic behavior until it reaches the critical temperature where the resistance drops at around 17 K, a characteristic of Bi-2201 superconductor. The zero resistance was not observed due to refrigerator limit.

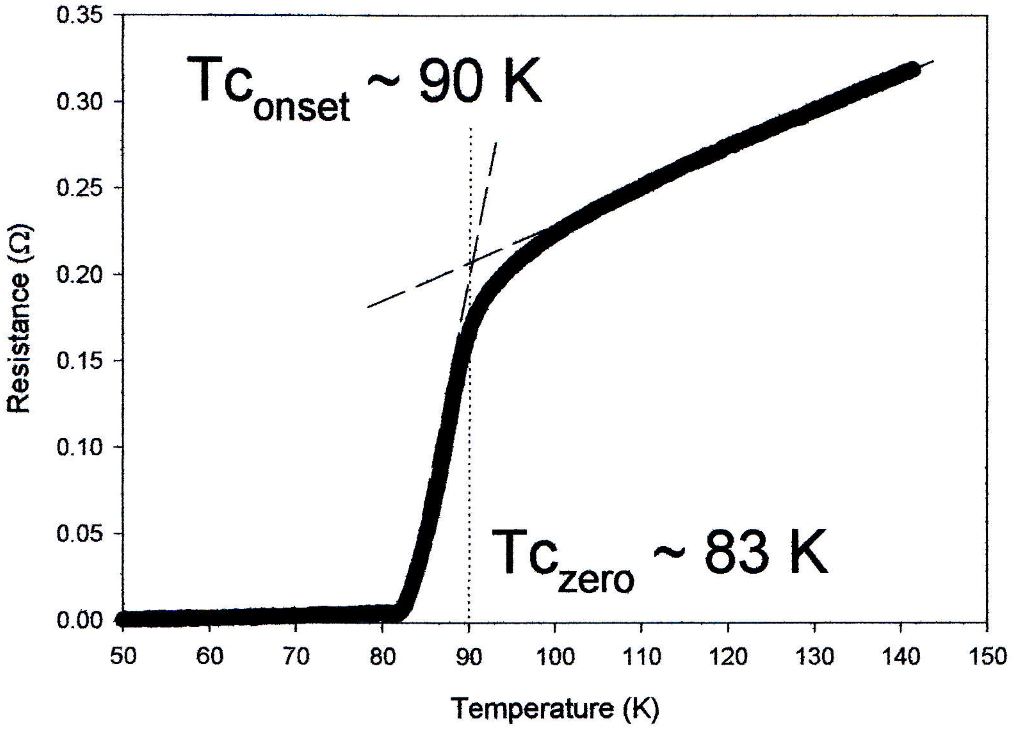

Figure 5.14. *Temperature dependence of resistance of Bi-2212 film. Tc$_{onset}$ is around 90 K and Tc$_{zero}$ around 83 K which results to a ΔTc of about 7 K.*

Figure 5.14 shows the resistance curve as a function of temperature for the Bi-2212 film. Note the sharp drop of resistance to zero at around 80 K, which is the critical temperature for the Bi-2212 superconductor. Deviation from the 80 K critical temperature can be attributed to the underdoping or overdoping of oxygen in the Bi-2212 material. Looking closely, the T_c onset is around 90 K and T_c zero around 83 K. This corresponds to the narrow transition width of about $\Delta T_c \approx 7$ K. This narrow transition width is comparable to the transition width of the single crystals [8] and thin films [9] of Bi-2212 obtained by other authors where transition widths are between 6 to 10 Kelvin.

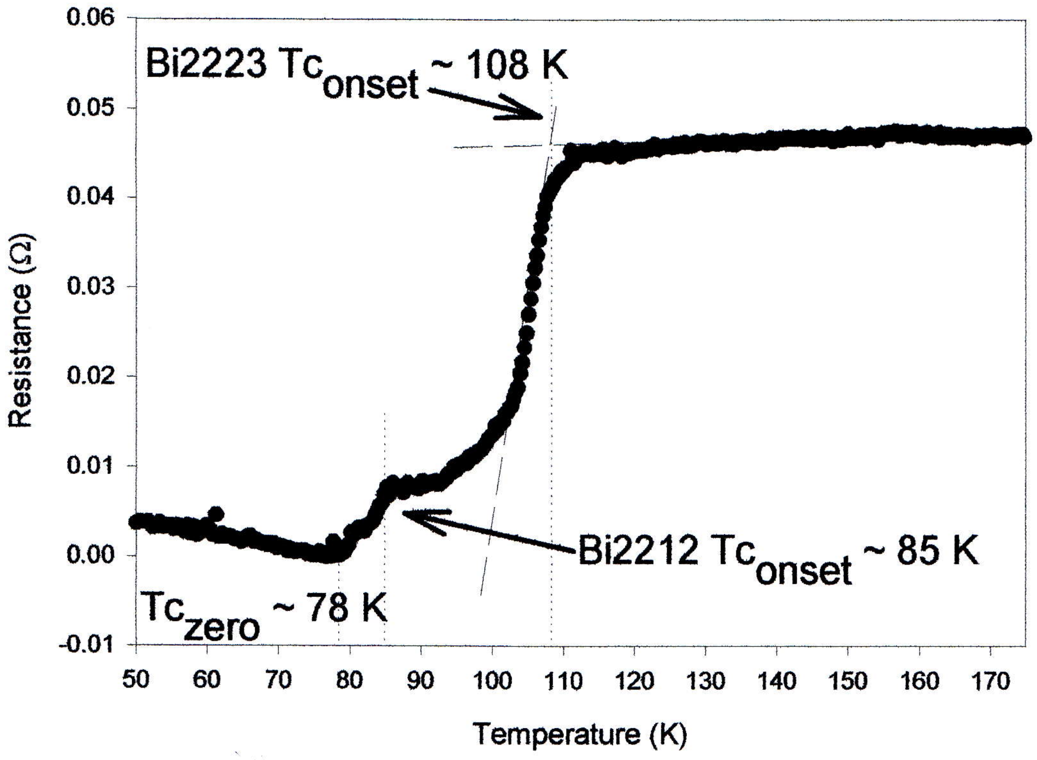

Figure 5.15. *Temperature dependence of resistance of multi-phase film composed of Bi-2212 and Bi-2223 film. $Tc_{Bi\text{-}2223}$ is around 108 K and $Tc_{Bi\text{-}2212}$ is around 85K.*

Figure 5.15 shows the temperature dependence of the resistance of multi-phase film composed of Bi-2212 and Bi-2223. It is observed that the resistance starts to drop at around 110K, which is the characteristic T_c of the Bi-2223 superconductor. However, due to the presence of Bi-2212 phase in the film, the resistance does not totally drop to zero. Another transition occurs which is the critical temperature for Bi-2212. This time, the resistance starts to drop at around 85 K and achieved the zero resistance at around 78 K. The relative drop of resistance for the multi-phase film doesn't necessarily suggest the relative amounts of each phase. The resistance drop is actually dependent on the path of the superconducting current on the film. Thus large drop of resistance at

108K doesn't suggest Bi-2223 as the dominant phase. From the XRD data, the dominant phase is the Bi-2212 material.

5.4 Mechanism of Film Growth and Alignment

From the initial loose powder characteristics of deposited powder on MgO, the resulting film after liquid phase sintering and annealing processes generally turns out to be aligned and textured with the absence of pores based on XRD measurement and SEM images. The initial stage in the development of the film during sintering process is the formation of liquid phase in the surface of grains as BSCCO materials melt incongruently [7]. From the phase equilibria diagram of BSCCO in Figure 2.2, incongruent melting occurs above 900°C, depending on the composition. At this temperature, BSCCO materials transform into a liquid phase, and solid phases $(Sr,Ca)CuO_2$ and Ca_2Cu_3 compounds [6]. This liquid wets and spreads to cover the solid surfaces. Soon after the formation of the liquid, the particles rearrange to produce a packing with some degree of stability. The partial melting continues which results to a redistribution of grains due to capillary stresses. The liquid causes particle rearrangement, resulting to densification. The surface energy provides the driving force in the initial formation of epitaxial layer. To lower the interfacial energy, the liquid segregates to surfaces of the grains and penetrate grain boundary, which includes the interface between the grains and the MgO substrate. The tendency of spreading, wetting and penetration result to elimination of pores, until further partial melting homogenizes the film surface. After partial melting, rearrangements occur until reprecipitation takes place by lowering the temperature to annealing temperature. Nucleation may start between the interface of the partially melted BSCCO and the MgO substrate. At this time, coarsening of the microstructure along with densification dominates, leading to the epitaxial formation of the BSCCO film on MgO substrate. An illustration of the film growth mechanism is shown in Figure 5.16.

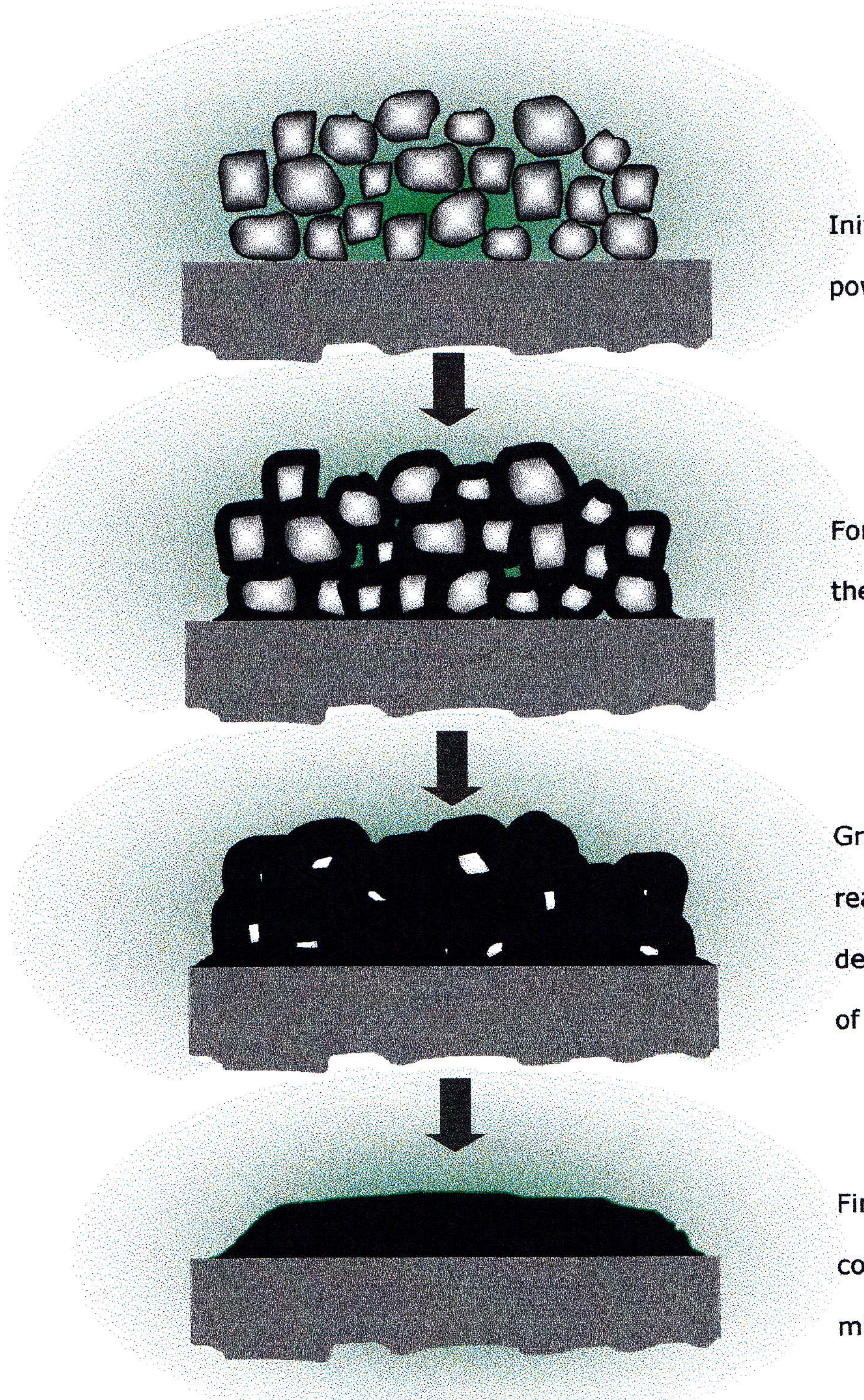

Initially loose deposited powder on MgO surface

Formation of liquid phase in the surface of BSCCO grains

Grain redistribution and rearrangemnet results to densification and elimination of pores.

Final densification and coarsening of the microstructure

Figure 5.16. *Mechanism of film growth during heat treatment via liquid phase sintering process*

Reference:

[1] B.D. Cullity, *Elements of X-Ray Diffraction*.

[2] R. Rössler, J.D. Pedaring, Ch. Jooss. Physica C, 361, 2001 p.18

[3] S. Kohli, C.D. Rithner, and P.K. Dorhout, *Xray Characterization of Annealed Iridium Films*, J. App. Phys., Vol. 91., No. 3., 2002 p. 1151

[4] A. Richter, R. Guico, J. Wang. Rev. Sci. Instrum., Vol. 72, No. 7, July 2001 p. 3005

[5] L. Albini, G. Carlotti, G. Gubbiotti, S. Loreti, C. Minarini, L. Palmieri, S.R. Teixeira, Physica B 275 (2000) 253}257

[6] P. Majewski, *Materials aspects of the high-temperature superconductors in the system BSCCO*. J. Mater. Res., Vol. 15, No. 4 Apr. 2000

[7] A. Bourdillon and N.X. Tan Bourdillon, *High Temperature Superconductors: Processing and Science*. Academic Press, Inc. USA, 1994, p. 85.

[8] S. Kishida. E. Hosokawa, *Optimum Growth condition of Bi-2212 single crystals in a vertical Bridgman method*. Journ. Of Crystal Growth 192 (1998) 138.

[9] H. Faqir, G. Vacquier, H. Chiba, M. Kikuchi, Y. Muraoka, and Y. Syono, *Growth of High Quality Bi-2212 single crystal and characteristics*, Journal of Material Research, Vol. 12, No.10, Oct. 1997.

Chapter 6
Conclusions and Recommendations

It was shown based on x-ray diffraction scan, electron microscopy, and resistivity measurements that *c*-axis oriented BSCCO films can be successfully grown on MgO (001) single crystal substrate by the combined method of powder deposition technique and heat treatment via liquid phase sintering process. A relatively pure phase films of Bi-2201 and Bi-2212 were produced while a multiple-phased film was obtained in an attempt to produce Pb-free Bi-2223. The difficulty of attaining single phase Bi-2223 is primarily due to the instability of the phase. The characteristics of the resulting films were shown to be comparable to that of grown by other methods.

A mechanism of film growth was also discussed based on the x-ray diffraction analysis and scanning electron microscopy. The incongruent melting of BSCCO materials that results to the presence of liquid phase during sintering process assists to densification and homogenization of the film.

Optimal growth shows the reproducibility of the *c*-axis oriented Bi-2212 film (refer to Appendix B) using the proposed method. While *c*-axis oriented Bi-2212 can be easily grown by this method, growth of single phased Bi-2223 still remains a challenging task.

The method that was just presented is a very promising technique in the fabrication of high quality superconducting films aside from BSCCO materials. While much of this work presents the viability of BSCCO materials with the method, preliminary result in the laboratory shows the capability of the method to produce *c*-axis YBCO superconducting film on $SrTiO_3$ (001) single crystal substrate (refer to Appendix C). Much effort still has to be done to be able to optimize each high T_c materials individually by this method.

It would also be interesting to study the effect of initial powder grain size in the fabrication of the films. Further investigation of the film thickness in relation to the amount of deposited powder can also be considered. Moreover, since the success in the growth of BSCCO films is dependent on the wetting and spreading of BSCCO material on MgO substrate, a study of surface reaction has to be conducted.

Appendix A
XRD Simulations

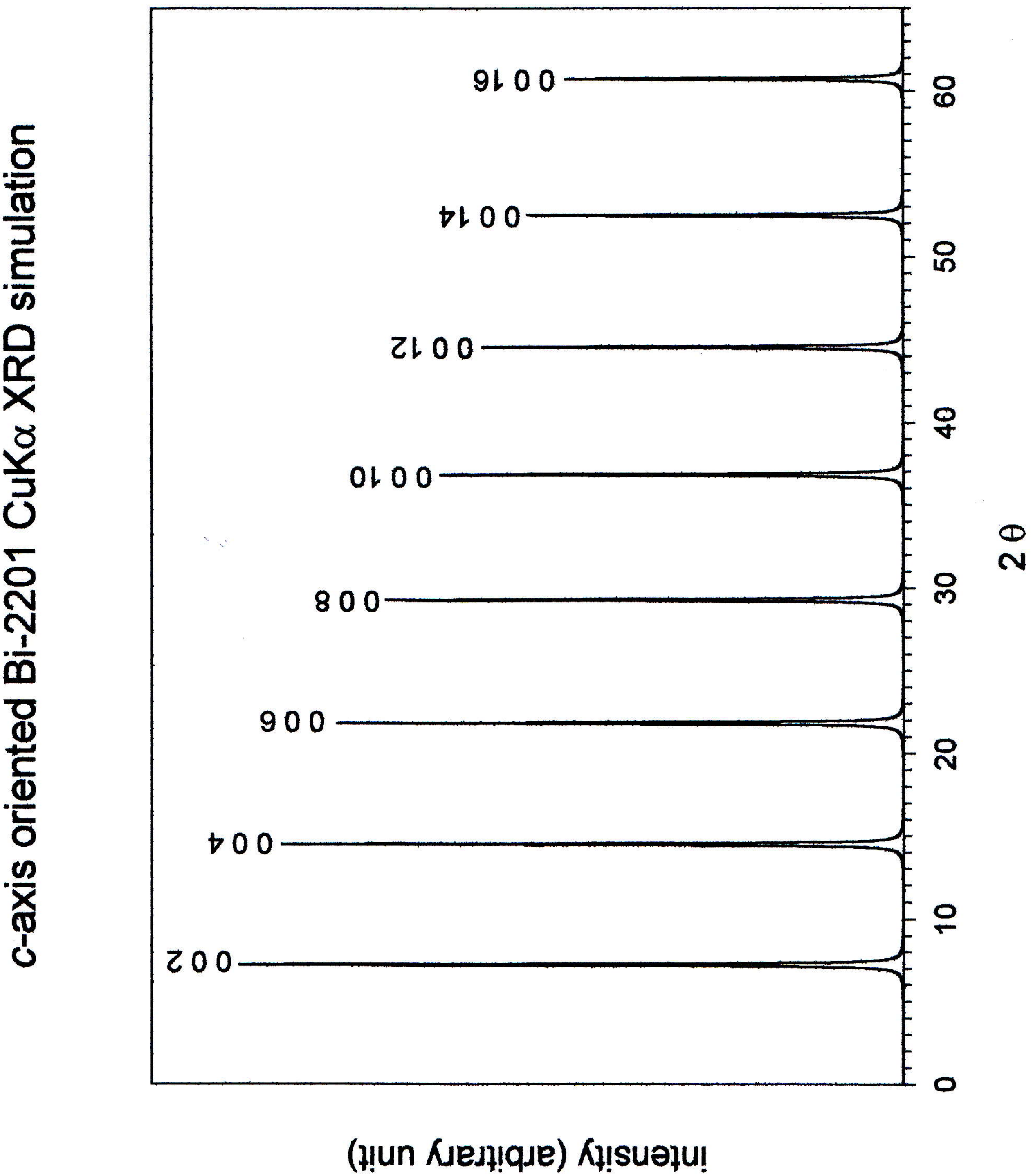
c-axis oriented Bi-2201 CuKα XRD simulation
0 0 2
0 0 4
0 0 6
0 0 8
0 0 10
0 0 12
0 0 14
0 0 16
intensity (arbitrary unit)
0
10
20
30
40
50
60
2θ

c-axis oriented Bi-2201 CuKα XRD simulation
with interfering peaks due to CuKβ radiation

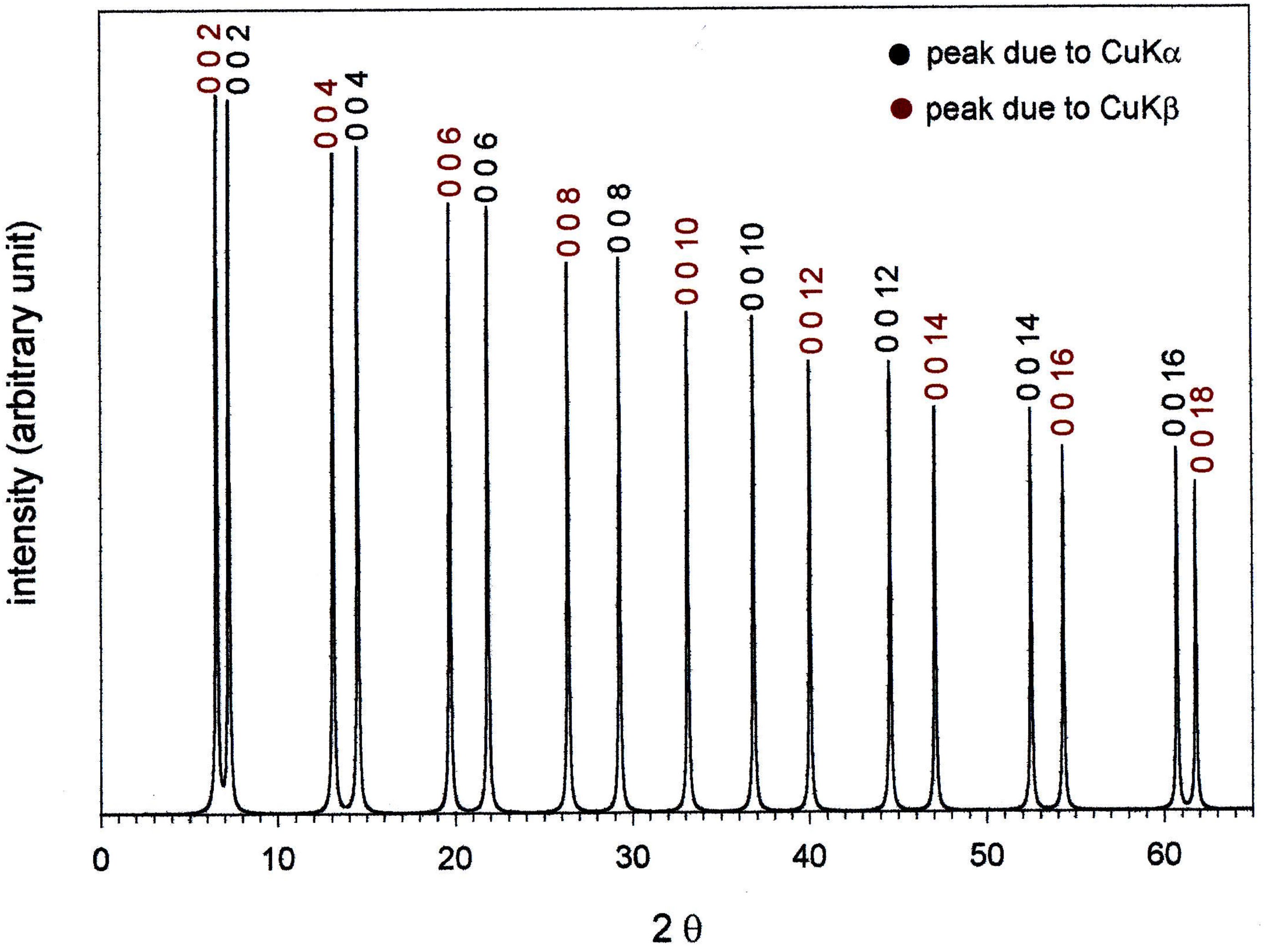

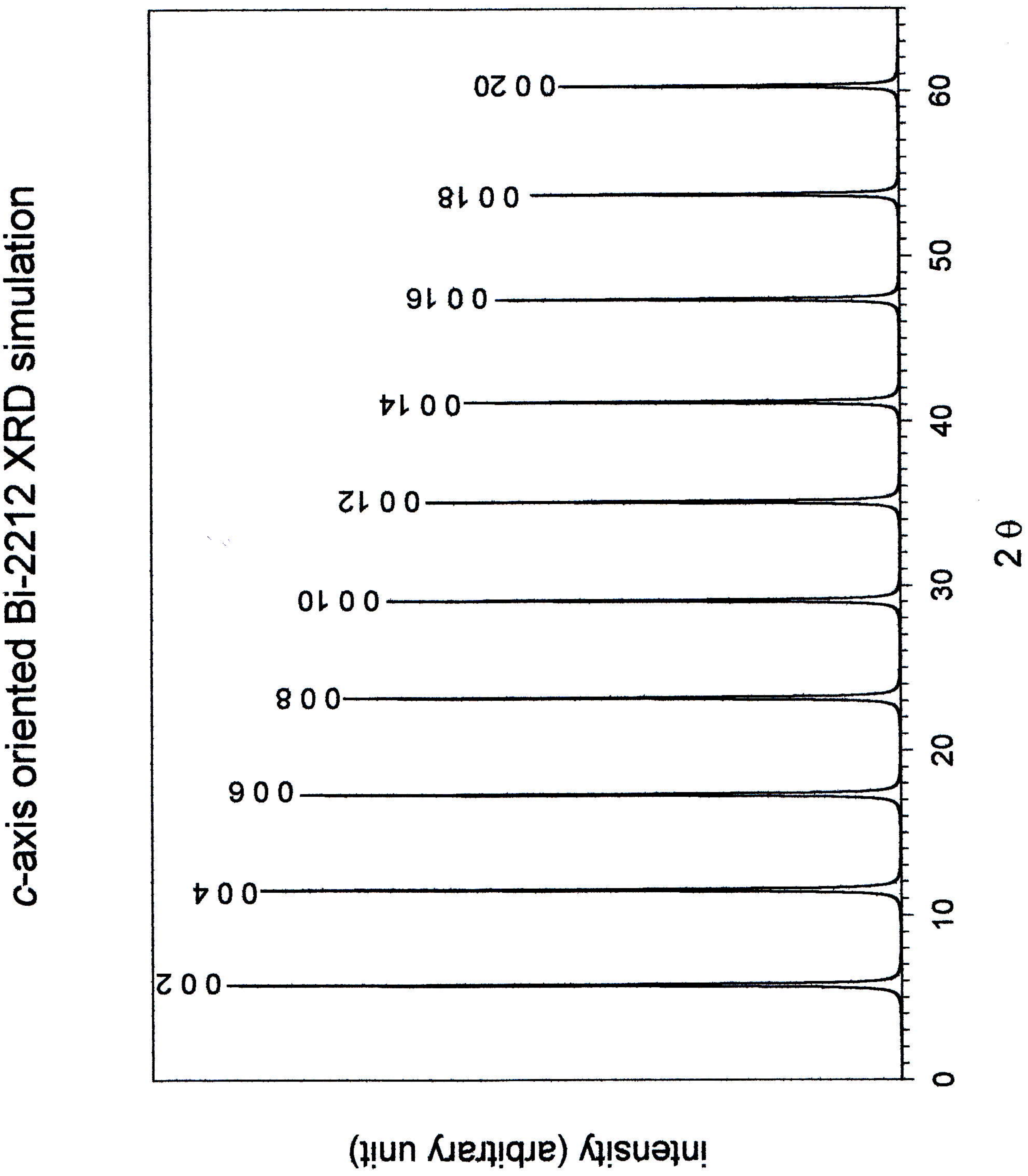
c-axis oriented Bi-2212 XRD simulation
0 0 2
0 0 4
0 0 6
0 0 8
0 0 10
0 0 12
0 0 14
0 0 16
0 0 18
0 0 20
0
10
20
30
40
50
60
2 θ
intensity (arbitrary unit)

c-axis oriented Bi-2212 CuKα XRD simulation
with interfering peaks due to CuKβ radiation

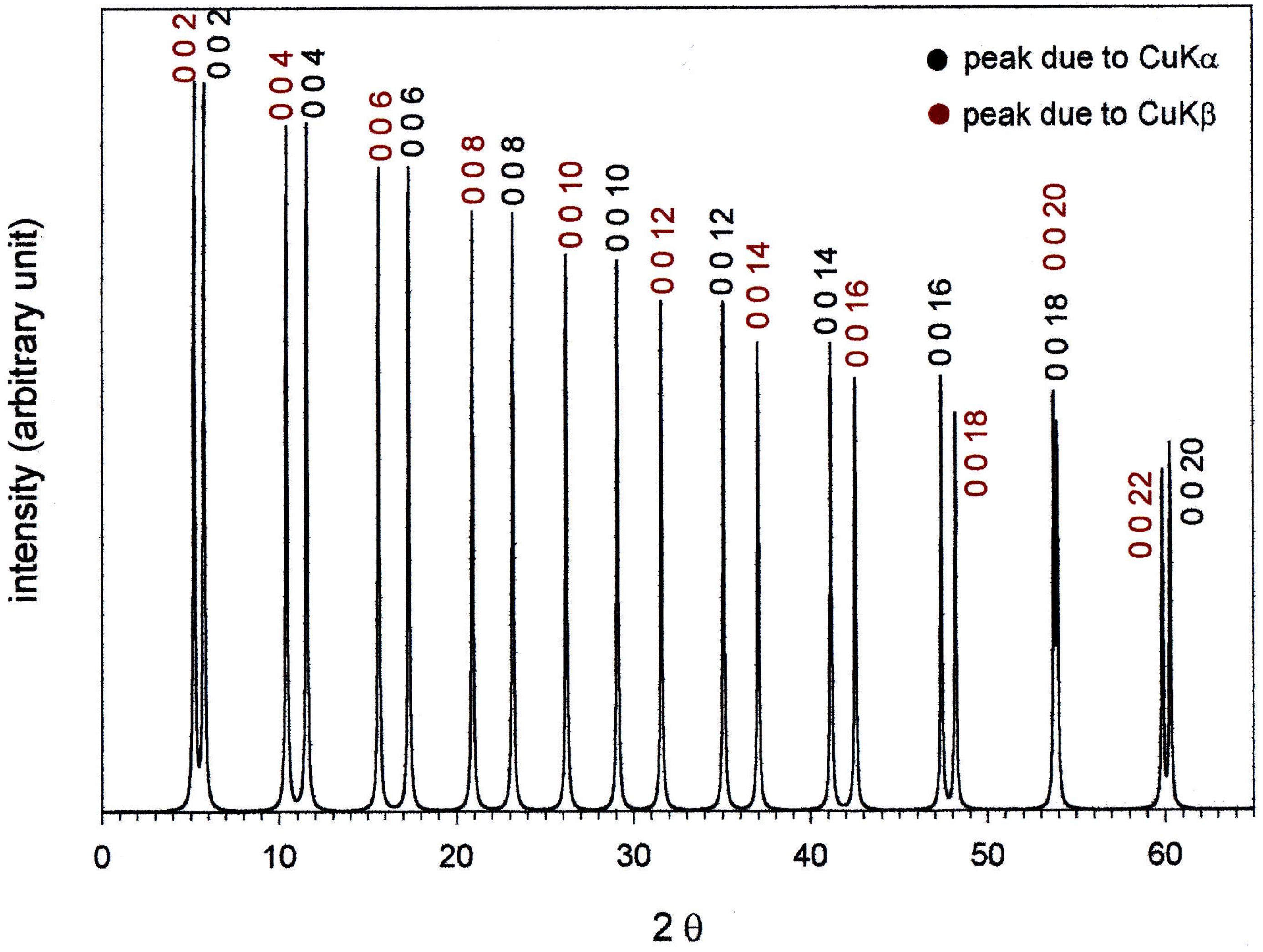

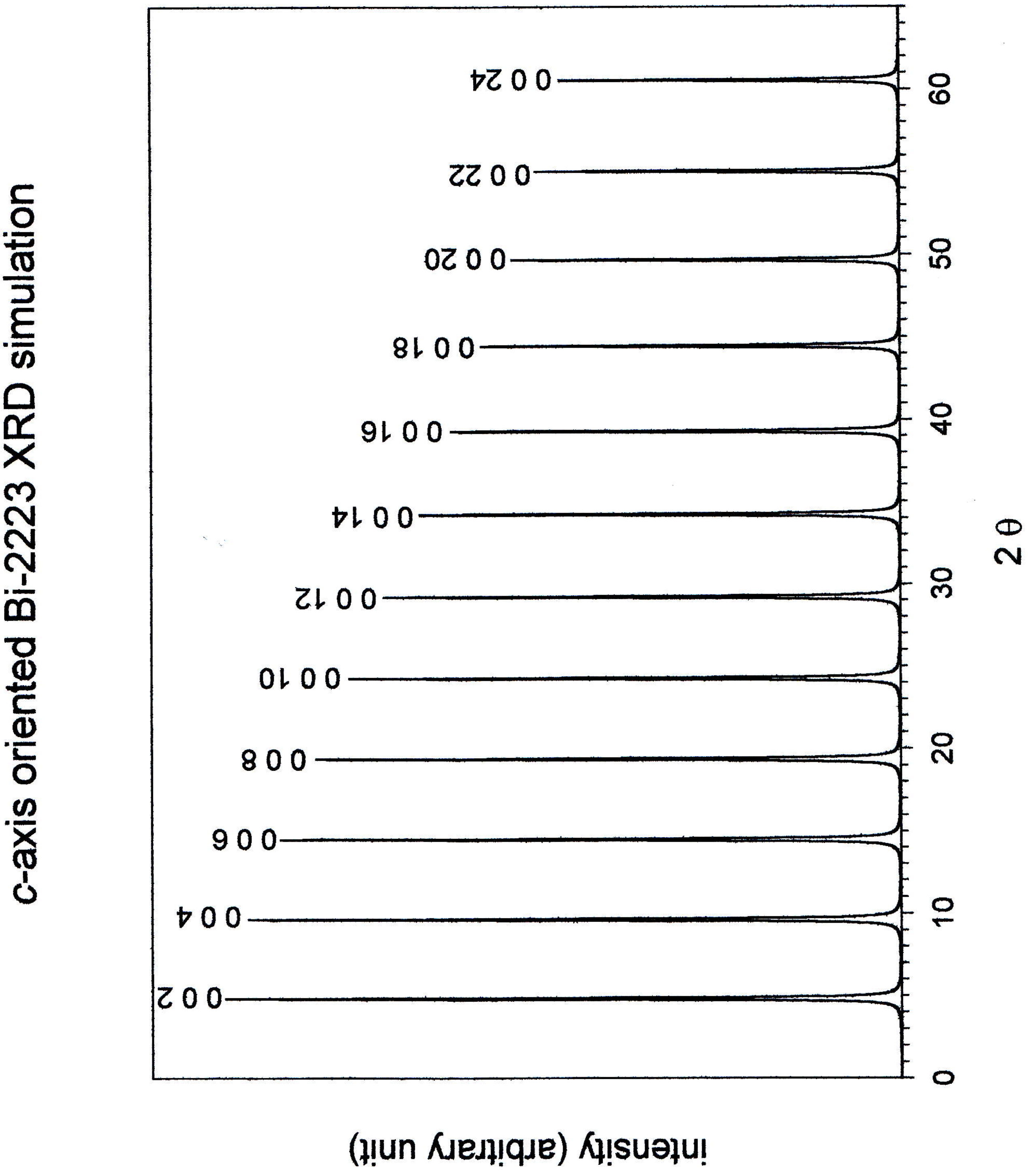
c-axis oriented Bi-2223 XRD simulation
0 0 2
0 0 4
0 0 6
0 0 8
0 0 10
0 0 12
0 0 14
0 0 16
0 0 18
0 0 20
0 0 22
0 0 24
0
10
20
30
40
50
60
2 θ
intensity (arbitrary unit)

c-axis oriented Bi-2223 CuKα XRD simulation
with interfering peaks due to CuKβ radiation

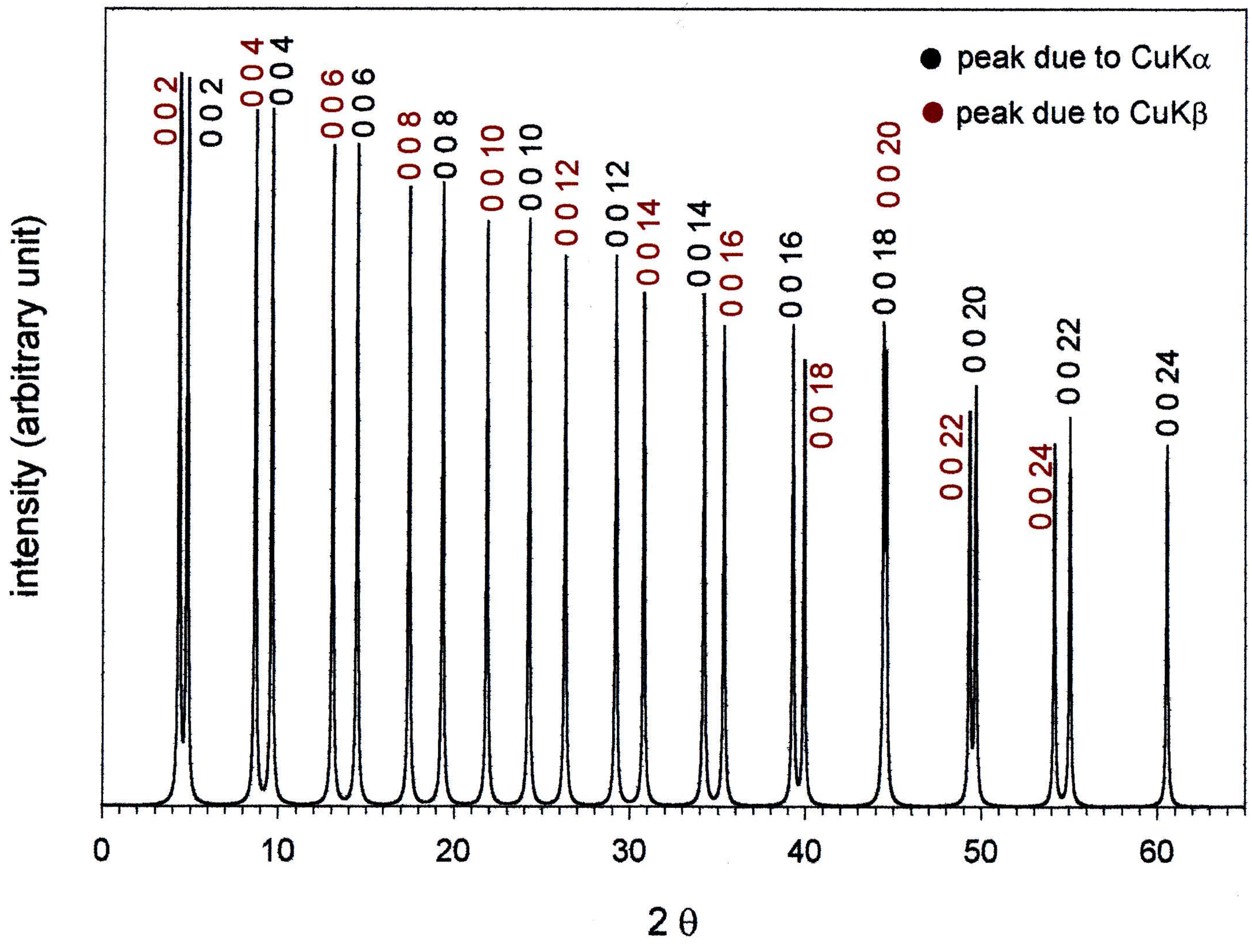

MgO (001) single crystal substrate XRD simulation

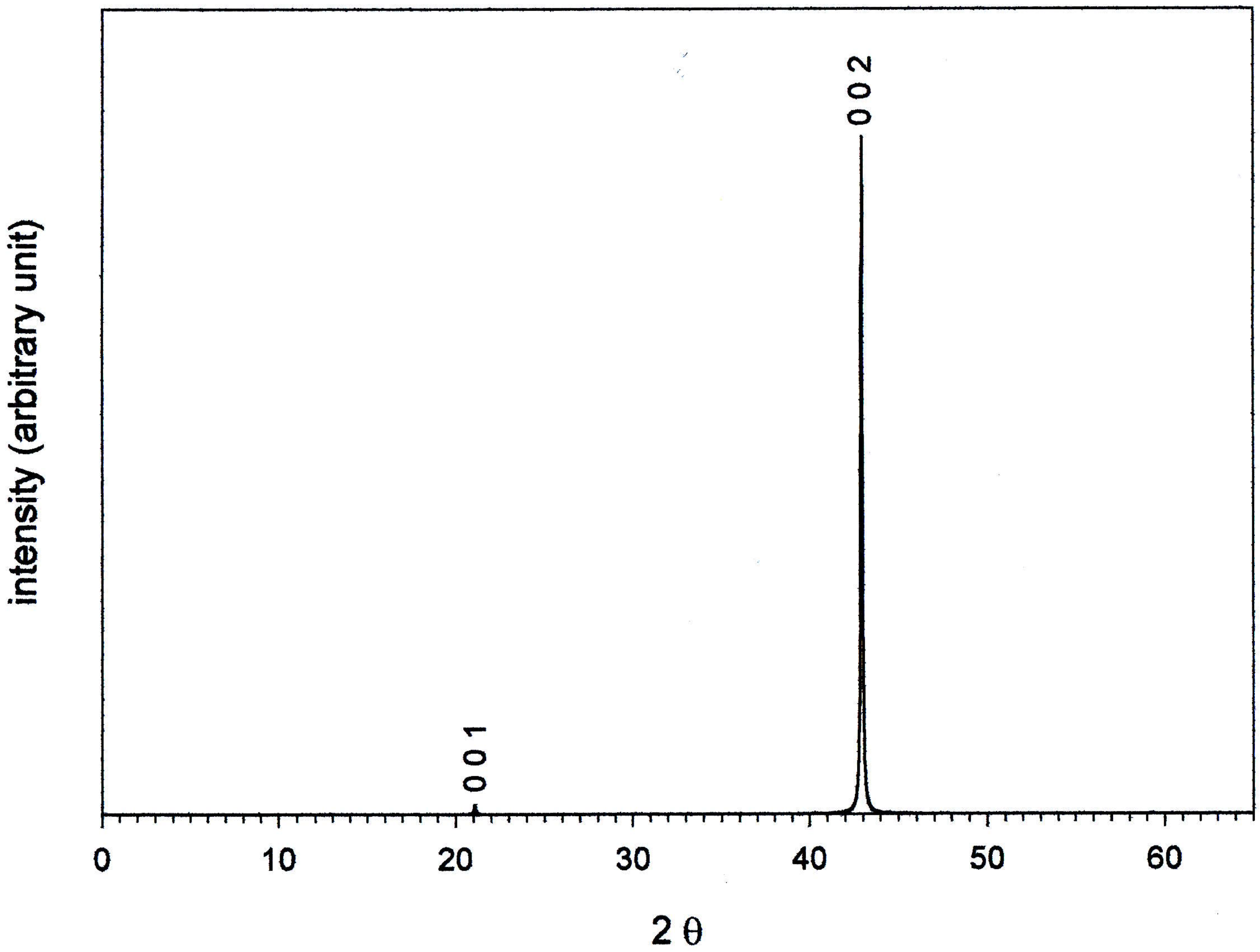

MgO (001) single crystal substrate CuKα XRD simulation
with interfering peaks due to CuKβ radiation

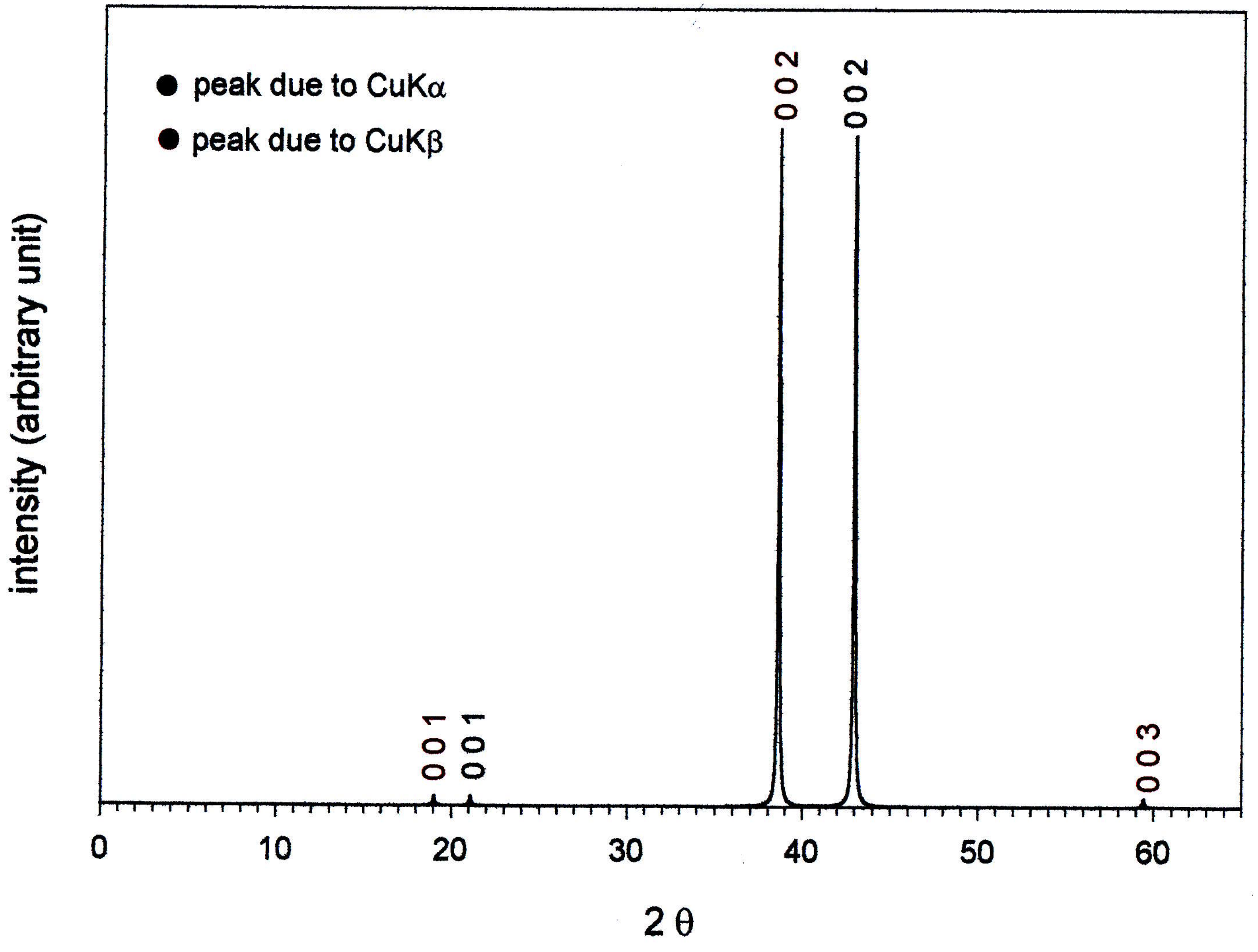

Fortran program code used in XRD simulation:

```
          implicit none
          real n,vol,alph,bet,gam,a,b,c,pi

          call volume(vol,pi,alph,bet,gam,a,b,c)
          print *, 'Enter number of basis of the crystal'
          read (*,*) n
          call xrd(vol,pi,alph,bet,gam,a,b,c,n)

          end

!********Calculation of unit lattice volume

          subroutine volume(vol,pi,alph,bet,gam,a,b,c)
          real a,b,c,alph,bet,gam,vol,pi

          print *, 'Enter primitive axes a,b,c'
            read (*,*) a
            read (*,*) b
            read (*,*) c
          print *, 'Enter angles alpha, beta, gamma'
            read (*,*) alph
            read (*,*) bet
            read (*,*) gam

          pi=3.141592653589
          alph=alph*pi/180.0
          bet=bet*pi/180.0
          gam=gam*pi/180.0

          vol=a*b*c*(sqrt(1.0-(cos(alph)**2.0)-(cos(bet)**2.0)-(cos(gam)**2.0)
     +      +(2.0*cos(alph)*cos(bet)*cos(gam))))

          end

!*********XRD simulation

          subroutine xrd(vol,pi,alph,bet,gam,a,b,c,n)
          real h,k,l,pi,alph,bet,gam,a,b,c,theta
          real S11,S22,S33,S12,S23,S13,Dd,n,bas(n,3.0)
          real Fcos,Fsin,FF,ctr
          real i,j
          real Atheta(1000),Ah(1000),Ak(1000),Al(1000),AFF(1000)
          character*32 fileth, fileh, filek,filel,fileFF
          real x,y,Ntheta(1000),NFF(1000),hkl(1000,3),atom(n)
          real af,polar

          real nn,mm,ll,data1(200),tester, data2(200),int,zz


          do i=1.0,n
          print *, 'Enter components of basis',i,' Press Enter after each
     + component!'
                    do j=1.0,3.0
                    read (*,*) bas(i,j)
                    end do
          print *, 'Enter atom in that basis. Enter atomic number'
                    read (*,*) atom(i)
          end do

          ctr=0.0
          do l=0.0,25.0                     ! start loop
          h=0.0
          k=0.0

          S11=(b**2.0)*(c**2.0)*(sin(alph)**2.0)
          S22=(a**2.0)*(c**2.0)*(sin(bet)**2.0)
          S33=(a**2.0)*(b**2.0)*(sin(gam)**2.0)
          S12=(c**2.0)*b*a*(cos(alph)*cos(bet)-cos(gam))
          S23=(a**2.0)*b*c*(cos(bet)*cos(gam)-cos(alph))
          S13=(b**2.0)*a*c*(cos(gam)*cos(alph)-cos(bet))

          Dd=((1.0/vol)**2.0)*(S11*h**2.0+S22*k**2.0+S33*l**2.0
     + +2.0*S12*abs(h)*abs(k)+2.0*S23*abs(k)*abs(l)
     + +2.0*S13*abs(h)*abs(l))

          theta=(360.0/pi)*(asin(1.54*sqrt(Dd)/2.0))   !1.39 for K-beta, 1.54 for K-alpha

          if(theta.lt.90.0) then

                    FF=0.0
                    Fcos=0.0
                    Fsin=0.0

                    do i=1.0,n

          call basatom(i,atom,n,theta,af)

          Fcos=Fcos+(cos((h*bas(i,1.0)+k*bas(i,2.0)+l*bas(i,3.0))*2.0*pi))*af
          Fsin=Fsin+(sin((h*bas(i,1.0)+k*bas(i,2.0)+l*bas(i,3.0))*2.0*pi))*af
                    end do
```

```
!        polar=(1.0+(cos(theta*(pi/180.0))**2.0))/(sin(theta*(pi/380.0))**2.0)
!     +       *(cos(theta*(pi/360.0)))
!        polar=(1.0/sin(theta*(pi/180.0)))
!     +       *(0.5*(1.0+((cos(theta*(pi/180.0)))**2)))

                   FF=(((Fcos)**2.0)+((Fsin)**2.0))*polar

         if(FF.gt.1.0) then
         ctr=ctr+1.0
         Atheta(ctr)=theta
         Ah(ctr)=h
         Ak(ctr)=k
         Al(ctr)=l
         AFF(ctr)=FF

!        print *, theta,h,k,l, FF,ctr            ! checking

         end if

         end if
         end do                        !end loop

         ctr2=0.0
         do x=1.0,ctr
         do y=1.0,ctr
         if(Atheta(x).eq.Atheta(y)) then
         Ntheta(x)=Atheta(y)
         NFF(x)=NFF(x)+AFF(y)
         end if
         end do
         ctr2=ctr2+1.0
         hkl(x,1)=Ah(x)
         hkl(x,2)=Ak(x)
         hkl(x,3)=Al(x)
         print *, Ntheta(x),hkl(x,1),hkl(x,2),hkl(x,3),NFF(x),ctr2
         end do

!!!!!!! Sorting data points

         nn=1.0
         data1(nn)=Ntheta(nn)
         data2(nn)=NFF(nn)
         nn=2.0
         do ll=2,ctr2
         tester=0
         data1(nn)=Ntheta(ll)
         data2(nn)=NFF(ll)
         do mm=1,nn-1.0
         if(data1(nn).eq.data1(mm)) then
         tester=1.0
         exit
         else
         continue
         end if
         end do
         if(tester.ne.(1.0)) then
         nn=nn+1.0
         end if
         end do

         do ll=1,nn
        if(data1(nn).eq.data1(ll)) then
         nn=nn-1.0
         exit
         else
         continue
         end if
         end do

         do ll=1,nn
         print *, data1(ll), data2(ll)
         end do

!!!!!! End of program "sorting data points"

!!!!!!!!!!!!!Creating XRD Graph


         do zz=0,90,0.01
         int=0
         do ll=1,nn-1.0
         int = int + (data2(ll)/(1.0+(((zz-data1(ll))/0.06)**2.0)))
         end do
         print *, zz, int
         end do

         end


!********* Basis atoms and atomic scattering factor database

         subroutine basatom(i,atom,num,theta,fnx)

         real i,atom(num),theta,fnx,x,B,C,N,O,Na,Mg,Si,Cl,K,Ca,Ti,Cu,Ga,Y
         real Hg, Ba, Bi, Sr
```

```
          x=(sin((theta/2.0)*(3.1415926535897/180.0)))/1.54

          if (atom(i).eq.5) then
          fnx = B(x)
          end if

        if (atom(i).eq.6) then
        fnx = C(x)
        end if

        if (atom(i).eq.7) then
        fnx = N(x)
        end if

        if (atom(i).eq.8) then
        fnx = O(x)
        end if

          if (atom(i).eq.11) then
          fnx = Na(x)
          end if

          if (atom(i).eq.12) then
          fnx = Mg(x)
          end if

        if (atom(i).eq.14) then
        fnx = Si(x)
        end if

        if (atom(i).eq.17) then
        fnx = Cl(x)
        end if

        if (atom(i).eq.20) then
        fnx = Ca(x)
        end if

        if (atom(i).eq.29) then
        fnx = Cu(x)
        end if

        if (atom(i).eq.38) then
        fnx = Sr(x)
        end if


          if (atom(i).eq.39) then
          fnx=Y(x)
          end if

          if (atom(i).eq.80) then
          fnx=Hg(x)
          end if

        if (atom(i).eq.83) then
        fnx = Bi(x)
        end if

          if (atom(i).eq.56) then
          fnx=Ba(x)
          end if

          end
!*********Atomic scattering factor database

        real function B(x)
        implicit none
        real x
        B=-(35.403*(x**6.0))+(108.72*(x**5.0))-(110.27*(x**4.0))
     +  +(24.62*(x**3.0))+(26.581*(x**2.0))-(18.35*x)+5.0102
        end

        real function C(x)
        implicit none
        real x
        C=-(117.37*(x**6.0))+(411.32*(x**5.0))-(535.68*(x**4.0))
     +  +(304.55*(x**3.0))-(55.826*(x**2.0))-(11.943*x)+6.0184
        end

          real function N(x)
        implicit none
        real x
        N=-(80.474*(x**6.0))+(304.65*(x**5.0))-(442.95*(x**4.0))
     +  +(297.29*(x**3.0))-(76.923*(x**2.0))-(7.2881*x)+7.0083
        end

        real function O(x)
        implicit none
        real x
        O=-(91.163*(x**6.0))+(350.26*(x**5.0))-(525.46*(x**4.0))
     +  +(376.38*(x**3.0))-(115.16*(x**2.0))-(1.4931*x)+8.0134
        end
     real function Na(x)
     implicit none
     real x
     Na=(49.02*(x**6.0))-(151.49*(x**5.0))+(155.26*(x**4.0))
+  -(48.87*(x**3.0))-(0.1697*(x**2.0))-(13.021*x)+10.997
     end

   real function Mg(x)
   implicit none
   real x
   Mg=-(57.87*(x**6.0))+(194.55*(x**5.0))-(251.35*(x**4.0))
+  +(155.72*(x**3.0))-(37.606*(x**2.0))-(13.452*x)+12.015
   end

   real function Si(x)
   implicit none
   real x
   Si=-(40.169*(x**6.0))+(94.001*(x**5.0))-(38.739*(x**4.0))
+  -(56.149*(x**3.0))+(62.413*(x**2.0))-(32.74*x)+14.01
   end

   real function Cl(x)
   implicit none
   real x
   Cl=-(256.67*(x**6.0))+(912.25*(x**5.0))-(1219.8*(x**4.0))
+  +(737.79*(x**3.0))-(172.13*(x**2.0))-(14.539*x)+17.028
   end

   real function Ca(x)
   implicit none
   real x
   Ca=-(135.45*(x**6.0))+(522.87*(x**5.0))-(766.16*(x**4.0))
+  +(515.91*(x**3.0))-(135.37*(x**2.0))-(17.446*x)+20.033
   end

   real function Cu(x)
   implicit none
   real x
   Cu=-(154.15*(x**6.0))+(611.42*(x**5.0))-(927.39*(x**4.0))
+  +(655.33*(x**3.0))-(188.05*(x**2.0))-(18.954*x)+29.024
   end

     real function Y(x)
     implicit none
     real x
     Y=-(213.71*(x**6.0))+(852.87*(x**5.0))-(1303.9*(x**4.0))
+  +(933.9*(x**3.0))-(280.16*(x**2.0))-(17.18*x)+39.021
     end

     real function Ba(x)
     implicit none
     real x
     Ba=-(244.45*(x**6.0))+(1003.4*(x**5.0))-(1586.5*(x**4.0))
+  +(1186.6*(x**3.0))-(381.66*(x**2.0))-(15.998*x)+56.014
     end

     real function Hg(x)
     implicit none
     real x
     Hg=-(151.57*(x**6.0))+(706.2*(x**5.0))-(1270.2*(x**4.0))
+  +(1081.4*(x**3.0))-(392.98*(x**2.0))-(25.007*x)+80.005
     end

     real function Sr(x)
     implicit none
     real x
     Sr=-(200.81*(x**6.0))+(804.74*(x**5.0))-(1234.5*(x**4.0))
+  +(885.52*(x**3.0))-(264.1*(x**2.0))-(18.455*x)+38.023
     end

     real function Bi(x)
     implicit none
     real x
     Bi=-(140.39*(x**6.0))+(665.96*(x**5.0))-(1217.5*(x**4.0))
+  +(1052.1*(x**3.0))-(386.59*(x**2.0))-(27.39*x)+83.022
     end
```

Appendix B
Reproducibility of Bi-2212 film

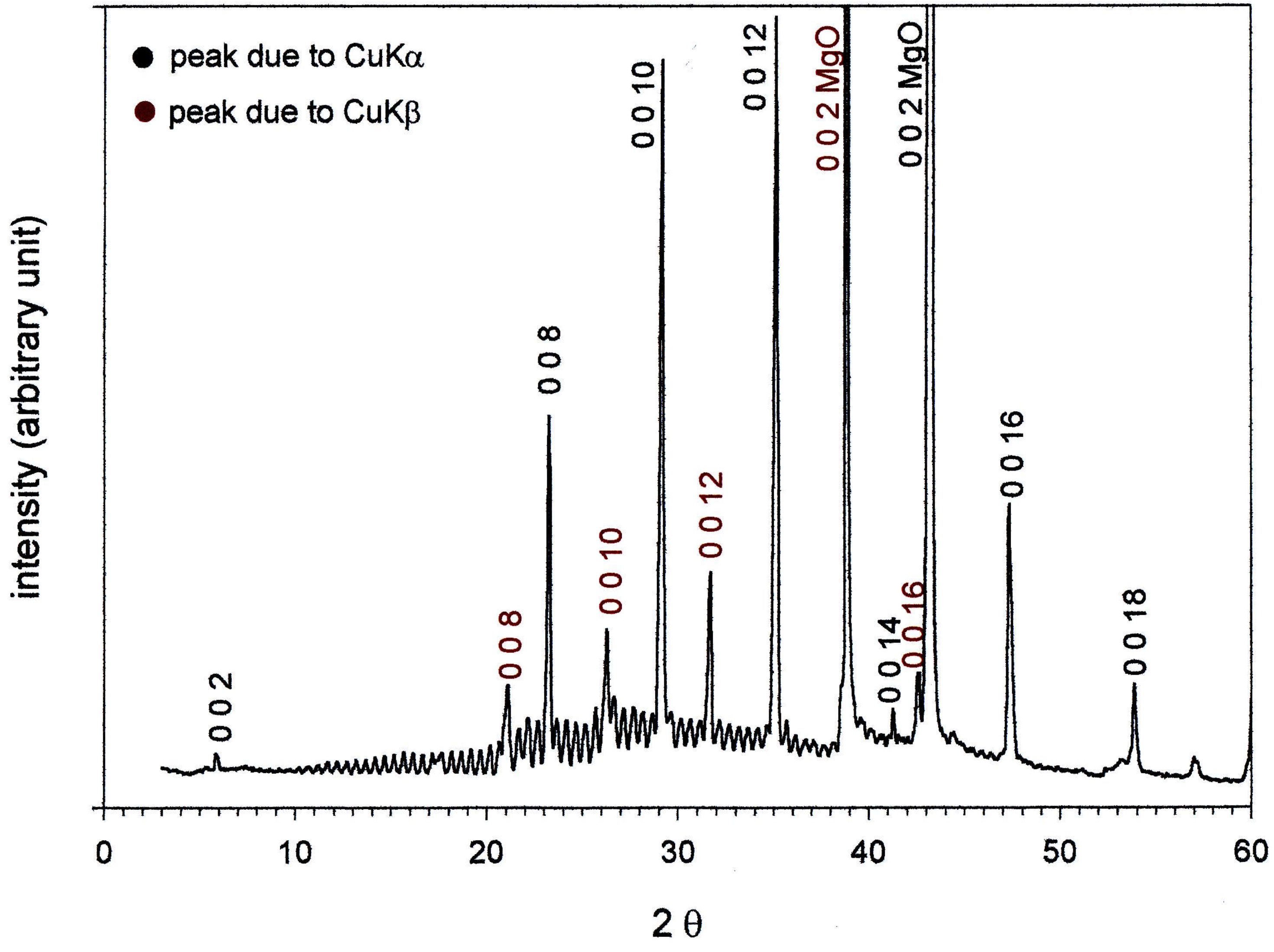

reproducible *c*-axis oriented Bi-2212 optimization growth

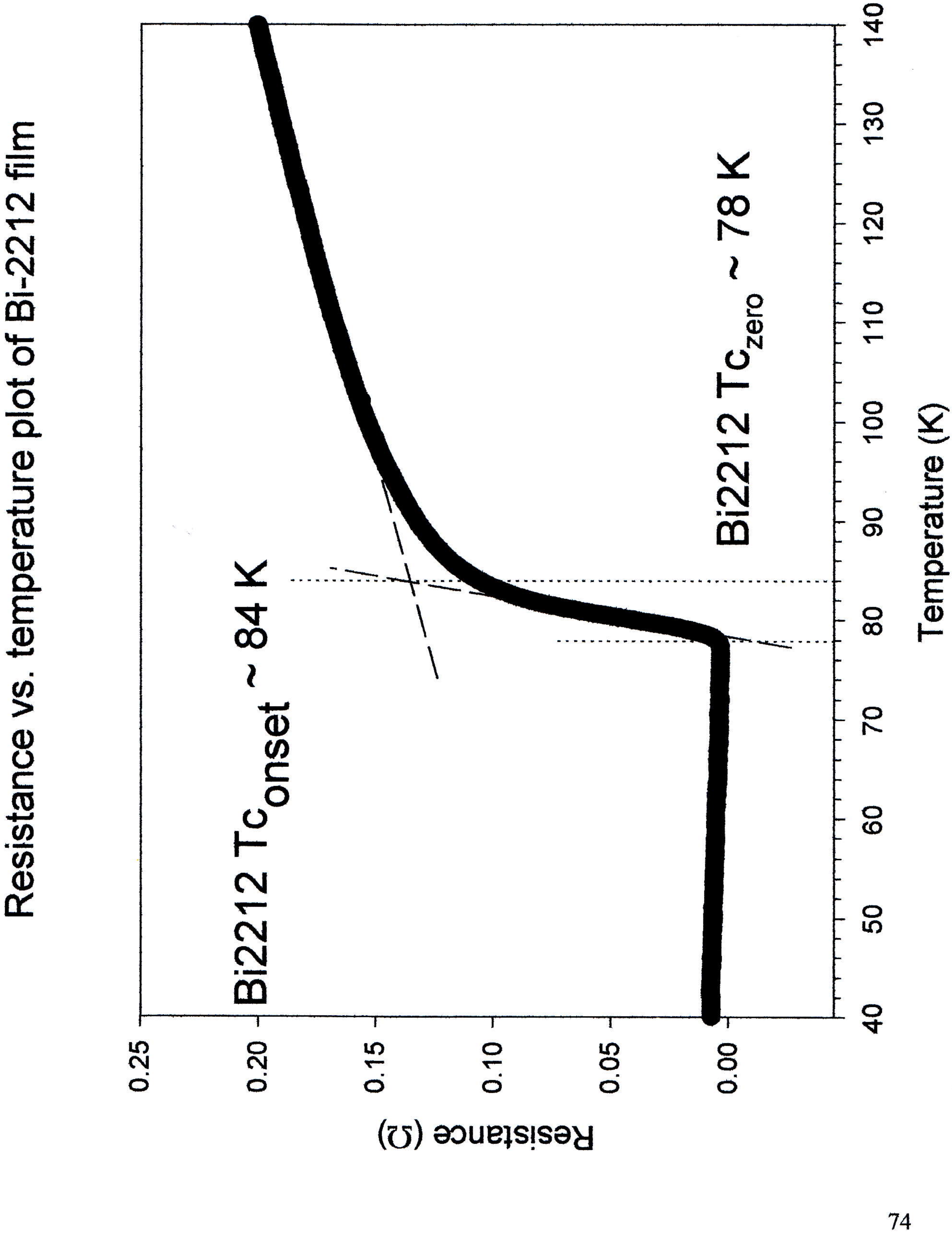
Resistance vs. temperature plot of Bi-2212 film
Bi2212 Tc$_{onset}$ ~ 84 K
Bi2212 Tc$_{zero}$ ~ 78 K
Resistance (Ω)
0.25
0.20
0.15
0.10
0.05
0.00
Temperature (K)
40
50
60
70
80
90
100
110
120
130
140

Appendix C
Preliminary result of *c*-axis oriented YBCO film grown by the method of combined powder deposition and heat treatment via liquid phase sintering process

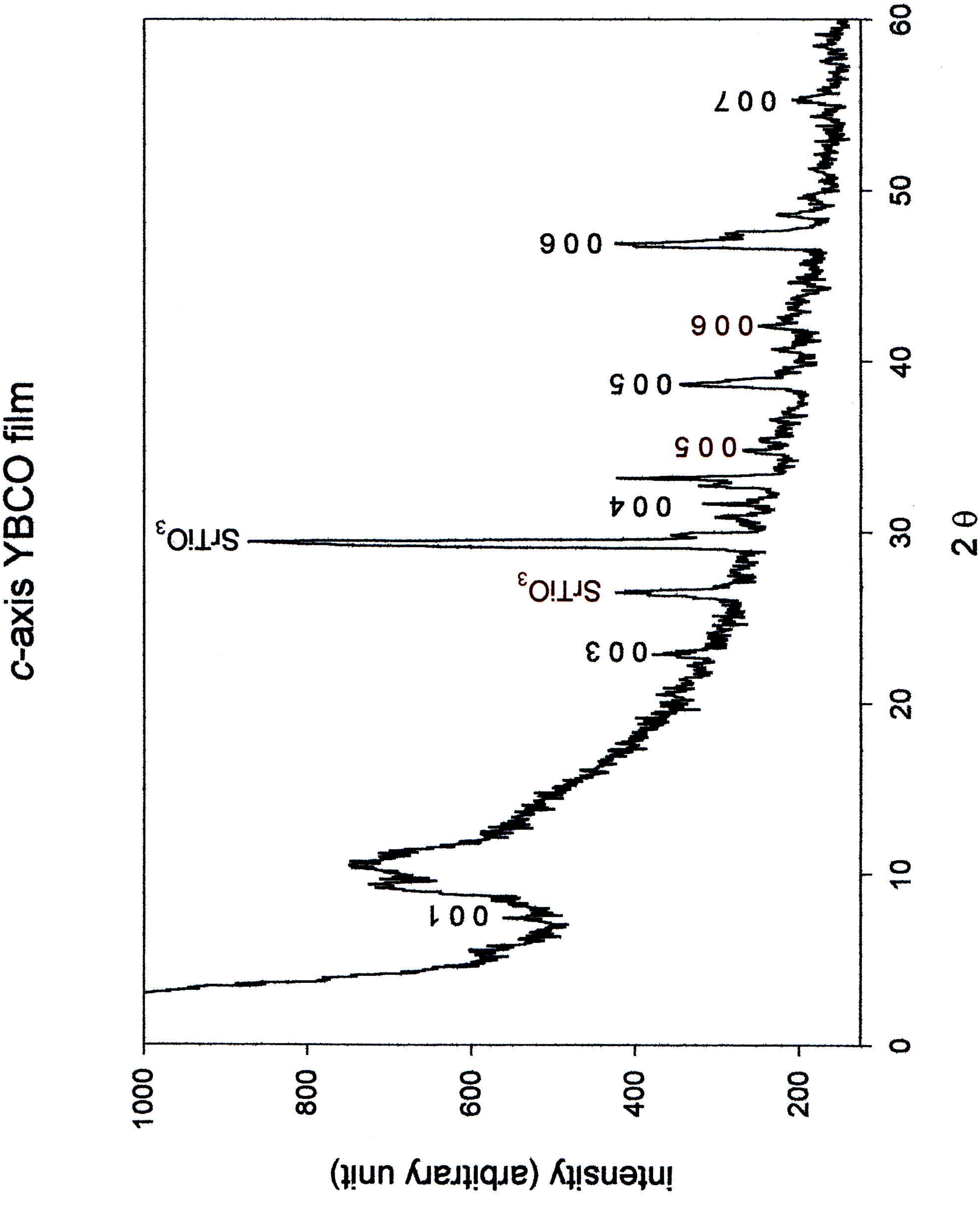
c-axis YBCO film
intensity (arbitrary unit)
1000
800
600
400
200
0
10
20
30
40
50
60
2 θ
0 0 1
0 0 3
SrTiO3
SrTiO3
0 0 4
0 0 5
0 0 5
0 0 6
0 0 6
0 0 7

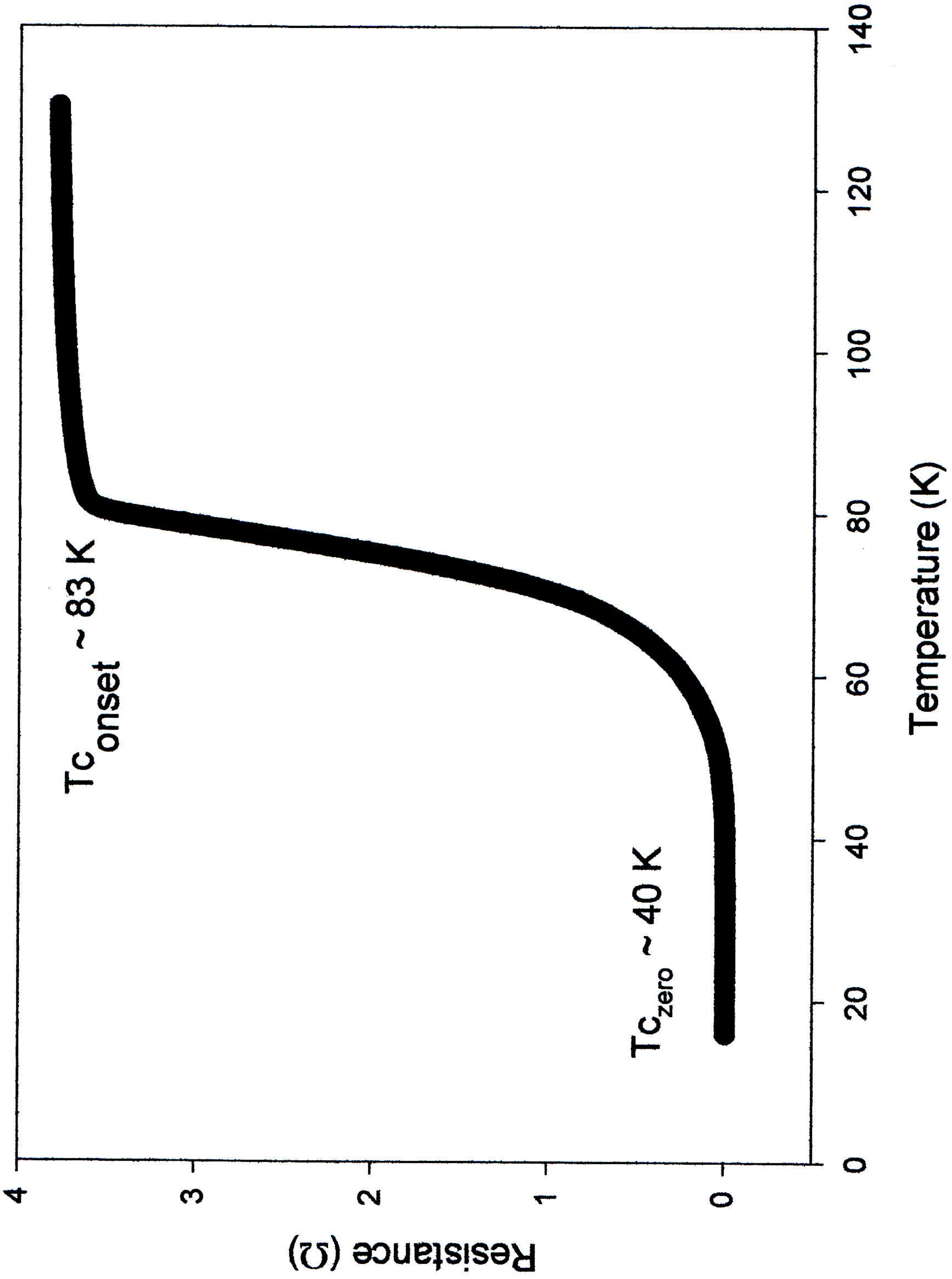

Resistance vs. Temperature plot of *c*-axis oriented YBCO film